

# SIMULATING DEEP HUBBLE IMAGES WITH SEMI-EMPIRICAL MODELS OF GALAXY FORMATION

MANUCHEHR TAGHIZADEH-POPP<sup>1,2</sup>, S. MICHAEL FALL<sup>1</sup>, RICHARD L. WHITE<sup>1</sup>, AND ALEXANDER S. SZALAY<sup>2</sup>

*Draft version July 3, 2018*

## ABSTRACT

We simulate deep images from the *Hubble Space Telescope* (*HST*) using semi-empirical models of galaxy formation with only a few basic assumptions and parameters. We project our simulations all the way to the observational domain, adding cosmological and instrumental effects to the images, and analyze them in the same way as real *HST* images (“forward modeling”). This is a powerful tool for testing and comparing galaxy evolution models, since it allows us to make unbiased comparisons between the predicted and observed distributions of galaxy properties, while automatically taking into account all relevant selection effects.

Our semi-empirical models populate each dark matter halo with a galaxy of determined stellar mass and scale radius. We compute the luminosity and spectrum of each simulated galaxy from its evolving stellar mass using stellar population synthesis models. We calculate the intrinsic scatter in the stellar mass-halo mass relation that naturally results from enforcing a monotonically increasing stellar mass along the merger history of each halo. The simulated galaxy images are drawn from cutouts of real galaxies from the Sloan Digital Sky Survey, with sizes and fluxes rescaled to match those of the model galaxies.

The distributions of galaxy luminosities, sizes, and surface brightnesses depend on the adjustable parameters in the models, and they agree well with observations for reasonable values of those parameters. Measured galaxy magnitudes and sizes have significant magnitude-dependent biases, with both being underestimated near the magnitude detection limit. The fraction of galaxies detected and fraction of light detected also depend sensitively on the details of the model.

*Subject headings:* galaxies: evolution — galaxies: formation — galaxies: fundamental parameters — galaxies: general — galaxies: statistics — large-scale structure of universe

## 1. INTRODUCTION

The *Hubble Space Telescope* (*HST*) has spent much of its operational lifetime staring into deep space, surveying galaxies in their infancy and youth. The motivation for these deep surveys (the Hubble Deep Field and its successors) was to obtain time-lapse images that would reveal how galaxies formed and evolved. While we have made great progress in interpreting the deep *HST* surveys, this program remains challenging and far from complete (Galametz et al. 2013; Guo et al. 2013b; Bouwens et al. 2014, and references therein). There are two major reasons for this. First, the samples of high-redshift galaxies have been severely edited by selection effects, primarily limits on flux and surface brightness, effectively biasing the observable universe toward bright, compact galaxies. Second, on the theoretical side, there are still many significant gaps in our understanding of the physical processes that affect the baryonic components of galaxies (stars, gas, and dust) and the radiation they emit. These uncertainties are reflected in the many free parameters of the semi-analytical models and in the analogous sub-grid physics of the hydrodynamical models. In this paper, we present a new approach to the analysis and interpretation of deep galaxy surveys that addresses both of these issues.

To account for selection effects, we create simulated *HST* images of model galaxy populations, and we then

analyze these images in the same way as real *HST* images, extracting catalogs from the simulated images to detect and measure the fluxes, sizes, and other properties of the galaxies. Our simulated images include both cosmological effects (projection along pencil beams, red-shifting of passbands, dimming of flux and surface brightness) and instrumental effects (point-spread function [PSF], pixelation, noise, sky backgrounds) for any given *HST* camera, filter, and exposure time. We then extract catalogs of objects in the images with the widely used SExtractor software (Bertin & Arnouts 1996). Thus, our procedure automatically takes into account all relevant selection effects, allowing us to make unbiased comparisons between the predicted and observed distributions of luminosities, sizes, and other properties of galaxies. This is the approach recommended by textbooks on statistical inference: map the predictions all the way into the observational domain and make the comparisons there, often called “forward modeling.”

The forward modeling method is not sensitive to small errors in the luminosities, sizes, and other properties of galaxies, or even to the exact definitions of these quantities, because such errors affect measurements of both the simulated and real images in the same way. In other words, these errors cancel out of the comparisons of the simulated and real distributions of luminosity, size, and so forth. This is one of the main advantages of the forward modeling approach.

In contrast, nearly all work in this field is based on the opposite, but simpler, approach of comparing predictions with observations in the theoretical domain (“back-

<sup>1</sup> Space Telescope Science Institute, 3700 San Martin Drive, Baltimore MD 21218, USA; mtaghiza@pha.jhu.edu

<sup>2</sup> Department of Physics and Astronomy, Johns Hopkins University, 3400 North Charles Street, Baltimore, MD 21218, USA

ward modeling”). Some exceptions are the reconstruction of mock images or data starting from semi-analytical models, (e.g. Blaizot et al. 2005; Overzier et al. 2013) or hydrodynamical simulations (e.g. Lotz et al. 2008; Devriendt 2010; Mozena 2013), although the latter suffer from unrealistic star formation histories and too rapid growth of stellar masses at early times (Bouche et al. 2010). In this paper, we go beyond the creation of mock galaxy images by deriving simulated distributions of galaxy properties and comparing them with the corresponding observed distributions.

To limit the number of assumptions and parameters in our models, we adopt a semi-empirical description of galaxy evolution. This description is based on the evolution of dark matter halos in cosmological  $N$ -body simulations, which is now well understood, in contrast to the evolution of the baryonic parts of galaxies. The main assumption of the semi-empirical description is that most of the information needed for simulating a population of galaxies is already encoded in the merger trees of their dark halos. Each halo is assumed to host one model galaxy, and the properties of that galaxy are then uniquely determined by those of its halo, including its mass and size. The advantage of this method is that it sidesteps much of the complex and uncertain baryonic processes in galaxy formation; the disadvantage is that it likely oversimplifies some aspects of these processes. This semi-empirical description has been developed in numerous studies over the past decade (e.g., Vale & Ostriker 2004; Conroy et al. 2006; Conroy & Wechsler 2009; Guo et al. 2010; Moster et al. 2010; Behroozi et al. 2010, 2013; Guo & White 2014; Moster et al. 2013; Kravtsov 2013; Reddick et al. 2013).

We derive the radiative spectrum of each simulated galaxy from its star formation history using stellar population synthesis models. The star formation history in turn follows from the growth of its halo mass, including both smooth accretion and discrete mergers with other halos. The radiative spectrum also depends on the metallicity of the stellar population and the absorption by gas and dust in the galaxy and by gas in the intergalactic medium.

In our implementation of this method, we use cutout images of real galaxies in the Sloan Digital Sky Survey (SDSS) as templates for the visual appearance of our model galaxies, with their fluxes and sizes rescaled to reflect galaxy evolution according to our models. This generates much more realistic morphologies than the smooth Sérsic bulge+disk light profiles commonly used in previous semi-empirical or semi-analytical models and improves modeling of the detection incompleteness effects that arise from the internal clumpiness of real galaxies.

Our approach gives us a valuable science tool for comparing models of galaxy evolution. In this paper we build a reference model using plausible choices of parameters, and explore other models by changing one parameter at a time. Thus, we can test the sensitivity of the simulated universe to each of these parameters by comparing the statistics derived from their respective simulated images to those from reference model and real *HST* images. Moreover, since the *input* properties of each model galaxy on the simulated images are known, we are able to quantify the model-dependent *output* galaxy detection efficiency by comparing the input and output distribu-

tions of galaxy properties (such as luminosity or size). Our approach can be used to inform the design of future surveys (e.g., choice of filters and exposure times) by addressing directly the question of which data are most useful to discriminate between different theoretical models. This will be especially valuable in planning the deepest surveys with the *James Webb Space Telescope* (*JWST*).

We emphasize that the main purpose of this paper is to demonstrate the validity and utility of a general method for analyzing and interpreting deep galaxy surveys. This is an initial, exploratory study. We regard our specific implementation of the method and the first results obtained from it and presented here as being illustrative rather than definitive. There is scope for further development of the method and refinement of the results. Nevertheless, the overall agreement we find between our simulations and observations—with no fine-tuning of parameters—is remarkable and encouraging.

This paper is arranged as follows. §2 explains the method for modeling and building simulated universes, from the selection of semi-empirical models and the dark matter simulation to the building of simulated *HST* images. The main results, presented in §3, include the implementation of stellar mass-halo mass relations (§3.1), present-day mass and luminosity distributions derived from the semi-empirical models of a simulated universe (§3.2), and a comparison of the luminosity, size and surface brightness distributions extracted from the simulated images with measurements from real *HST* images (§3.3). We devote §4 to an analysis of the cosmic star formation rate density. Lastly, §5 discusses the results and summarizes our conclusions.

## 2. BUILDING A SIMULATED UNIVERSE

In this section we describe in detail the steps required to build a self-consistent simulated universe and associated *HST* images. We also describe the parameters chosen for our *reference model* for the universe, as well as variations on those parameters explored in the other models.

### 2.1. The Dark Matter Simulation

Following standard practice, we use a  $\Lambda$ CDM simulation as the three-dimensional (3-D) skeleton of our simulated universes, placing a *model galaxy* at the center of each dark (sub)halo<sup>1</sup>. That defines the spatial distribution and number density of galaxies as a function of redshift. Most of the information needed in our method is in fact provided by the halo mass and size evolution along halo merger trees, which does not involve any fitting of free parameters (see §2.2 and §2.4).

For the merger trees, we use the milli-Millennium cosmological dark matter simulation (mMS) (Springel et al. 2005; Lemson & Springel 2006). Its smaller size compared to the full Millennium or Millennium II simulations (Springel et al. 2005; Boylan-Kolchin et al. 2009) makes it easier to use for this exploratory work; we show below that the coarser mass resolution in the mMS is adequate for our simulations (§3.3.1). Halos are defined using friends-of-friends groups as explained in Guo et al.

<sup>1</sup> We use “halo” and “sub-halo” interchangeably, following Guo et al. (2010).

(2010). Bound dark matter structures or (sub)halos are composed of the most massive main (or central) sub-halo surrounded by satellite sub-halos.

The mMS has the same cosmology and particle mass ( $1.18 \times 10^9 M_\odot$ ) as the much larger Millennium simulation, but with both a smaller box size (85.62 Mpc) and a reduced number of particles ( $270^3$ ). The cosmological parameters used are the ones obtained by *WMAP1* (Spergel et al. 2003), i.e.,  $\Omega_M = 0.25$ ,  $\Omega_\Lambda = 0.75$ ,  $h_0 = 0.73$  and  $\sigma_8 = 0.9$ . As explained by Guo et al. (2013a), the difference between the *WMAP1* and the standard *WMAP7* (Komatsu et al. 2011) cosmologies does not affect significantly the relevant aspects of dark matter structure. In fact, a smaller *WMAP7*  $\sigma_8 = 0.807$  is counterbalanced by a greater  $\Omega_M = 0.272$ , which results, for example, in the *WMAP1* and *WMAP7*-derived halo mass functions being very similar at  $z = 0$ .

## 2.2. Constructing Stellar Mass-Halo Mass Relations with an Intrinsic Scatter

We obtain the stellar mass of model galaxies in the simulation using semi-empirical modeling. This approach defines the stellar mass  $M_s$  of the galaxy as a function of the dark matter mass of the halo,  $M_s = M_s(M_{\text{halo}})$ , with the function  $M_s(M_{\text{halo}})$  defined to be the stellar mass-halo mass (SMHM) relation. Although this is a simple one-to-one relation, it can be readily modified to include statistical scatter or redshift dependence (e.g., Behroozi et al. 2013). In this paper we adopt several SMHM relations from the literature, and use them for building our simulated images. We introduce a novel, self-consistent approach that naturally adds scatter to the SMHM mass relation.

As a measure of the halo mass, we use the virial mass  $M_{\text{vir}}$  (mass enclosed inside the maximum radius within which the mean density is 200 times the critical value), which is obtained from the value-added catalog of Guo et al. (2010) based on the milli-Millennium simulation. In this catalog, the mass of a central halo is given by  $M_{\text{vir}}$ , whereas for a satellite halo it is the maximum  $M_{\text{vir}}$  ever attained before becoming a satellite. In the semi-empirical approach, this preserves the stellar mass of satellite galaxies even while the outer parts of their dark halos are being tidally stripped as they orbit within a central halo.

Figure 1 shows some of the SMHM relations found in the literature. Our reference model (or Model 1) for simulating the universe uses the redshift-independent SMHM relation from Guo et al. (2010). They computed this relation using a halo abundance matching technique that equates quantiles of the low redshift stellar mass function from SDSS (Li & White 2009) to those of the present-day halo virial mass function from the Millennium simulations. The quantile matching is made over a range of masses around the typical value  $M^*$  (i.e., the “knee” in the SMHM relation as well as in the mass function), with extrapolations to the very low and high mass regimes, where both the stellar and halo mass distributions are not well constrained. Another option is the redshift-evolving SMHM relation of Behroozi et al. (2013). This relation is based on stellar mass functions and cosmic star formation rates up to  $z = 8$ . For our non-evolving Model 2, we adopt the Behroozi et al. (2013) SMHM relation evaluated at  $z = 0$ , while for our evol-

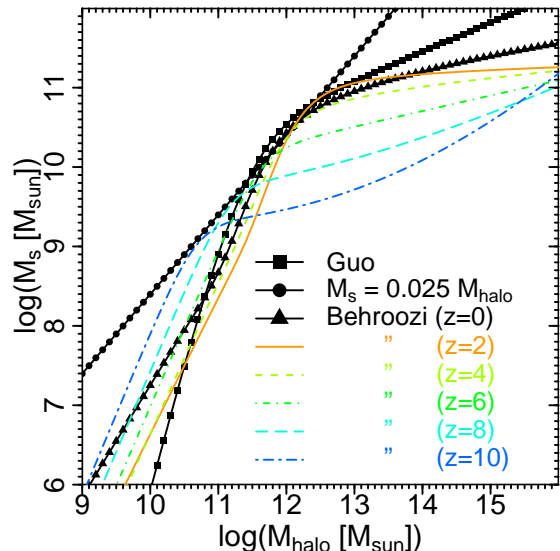


FIG. 1.— Stellar mass  $M_s$  versus halo mass  $M_{\text{halo}}$  relations tested in this paper. Included are the models of Guo et al. (2010) and Behroozi et al. (2013), as well as a linear SMHM relation  $M_s = 0.025 M_{\text{halo}}$ . The low and high mass tails are necessarily extrapolations of the fits due to the limited resolution of the DM simulations ( $\log M_{\text{halo}} < 10.8$  for the Guo et al. (2010) model and  $\log M_{\text{halo}} < 10.3$  for the Behroozi et al. (2013) model). Note that this last model evolves with redshift, with  $M^*$  (characterizing the knee in the SMHM relation) becoming smaller at higher redshift.

ing Model 3, we adopt the full redshift dependence of the Behroozi et al. SMHM relation. Our Model 4 does not involve halo abundance matching, but is a simple linear relation given by  $M_s = 0.025 M_{\text{halo}}$ , where the slope has been chosen by eye to coincide with the other relations in the vicinity of  $M^*$ . We include this last model not because it is realistic but to study the sensitivity of our results to a SMHM relation that is very different from those of our first three models (based on the results of Guo et al. 2010 and Behroozi et al. 2013).

In this paper, we do not explicitly impose random scatter in the SMHM relation. Instead we explore the scatter that emerges naturally from the dark matter simulation as a consequence of one basic assumption: *we assume that the stellar mass along merger trees is a monotonically increasing function of time*. This is physically plausible because the stellar mass is concentrated in the center of halos due to dissipation in the baryons, and as a result it tends to be retained during mergers. This is the simplest physically motivated rule we have found for creating consistent galaxy stellar masses from dark matter simulations. The alternative is to assume that galaxies lose and gain mass willy-nilly as halo masses decrease and increase and as sub-halos merge; that appears much less plausible based on our current understanding of galaxy formation and dynamics. Another alternative is to impose scatter on the SMHM relation in a predetermined manner (as in the approach adopted by Behroozi et al. (2013)).

Our assumption of monotonically increasing stellar mass naturally leads to scatter in the SMHM relation as a consequence of the following three related effects:

1. In dark matter simulations, individual halos can decrease in mass from one time step to the next,

for example in events of tidal stripping. In that case, we follow the approach of Guo et al. (2010) and do *not* reduce the stellar mass accordingly, but retain the stellar mass present before the decrease in  $M_{\text{halo}}$ .

2. In halo mergers, the dark matter mass of a descendant  $M_{\text{halo,desc}}$  can be smaller than the sum of the progenitor dark matter masses  $\Sigma M_{\text{halo,prog}}$  as some particles become unbound during the collision. This is not a rare occurrence in the simulations. In order to conserve the stellar mass content, we must break with the one-to-one fixed SMHM relation.
3. Observed SMHM relations are intrinsically non-linear (see Figure 1). That leads to a conflict with the assumed monotonic growth of  $M_s$  in halo mergers. Consider the case when two halos with  $M_{\text{halo,prog}} \sim M_{\text{halo}}^*$  merge to create a new halo with  $M_{\text{halo,desc}} > M_{\text{halo}}^*$ . The SMHM relation increases more slowly than linearly above  $M_{\text{halo}}^*$ , which means that  $M_s$  for the new halo is supposed to be smaller than the sum of the stellar masses for the merging halos. That conflicts with the assumption that the stellar mass along the merger tree must increase monotonically.

To eliminate these conflicts we adjust stellar masses retroactively as follows. If a halo is found to have a stellar mass (according to the imposed SMHM relation) that decreases with time, we decrease the stellar masses of its immediate progenitors to enforce a monotonic increase in the stellar mass content of dark matter halos across their merger trees. This adjustment is applied recursively to all the progenitors of halos with modified stellar masses. Note that we are not assuming reverse causality with this scheme! Our assumption is that lower mass halos in denser environments (which are going to merge in the future) have their star formation rates suppressed by these environments. This procedure is described in more detail in Appendix A.

One natural consequence of this procedure is that, at a given halo mass, there is a scatter in the stellar masses that tends to fall slightly below the one-to-one SMHM relation at some points in the merger history. The results with the modified SMHM relations will be shown in §3.1.

### 2.3. Illuminating Galaxies in Dark Matter Halos

The luminosity and spectrum of a model galaxy at any time are determined by its star formation history computed along the past merger history of its host dark matter halo. Star formation is implied when the stellar mass of a descendant halo is greater than the total stellar mass of its progenitors in consecutive simulation time steps, or when a single halo increases its dark matter mass (and hence its stellar mass) due to accretion of surrounding dark matter particles. The stellar mass increase between simulation time steps implies a star formation rate, which is used in stellar population synthesis models to compute the emitted spectrum of the galaxy. We assume that the star formation rate between time steps is uniform, so that the star formation history is completely determined by the stellar mass history of a halo. Note that since we

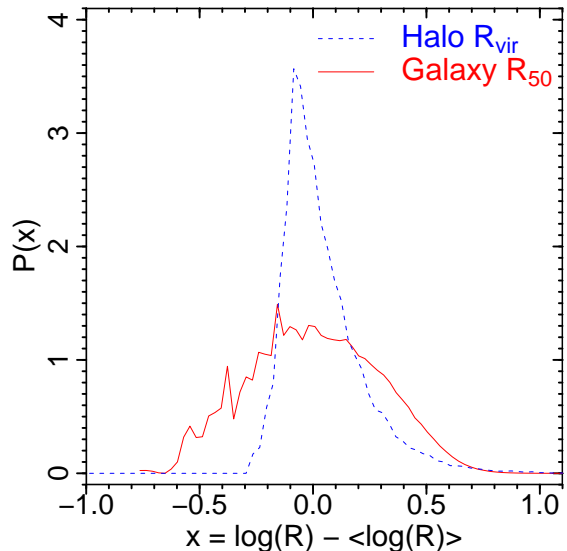


FIG. 2.— Probability density distributions of the (median subtracted) logarithms of  $R_{\text{vir}}$  (dark matter halo virial radius) and  $R_{50}$  (SDSS galaxy  $r$ -band half-Petrosian-flux radius). Note that the radius distributions resemble Gaussian curves, as expected for approximately log-normal random variables. The median values are  $\langle \log R_{\text{vir}} [\text{Mpc}] \rangle = -1.159$  and  $\langle \log R_{50} [\text{Mpc}] \rangle = -2.824$ , with standard deviations  $\sigma(\log R_{\text{vir}} [\text{Mpc}]) = 0.176$  and  $\sigma(\log R_{50} [\text{Mpc}]) = 0.285$ .

have forced the stellar mass to increase monotonically with time, negative star formation rates are automatically excluded.

We thus simply reconstruct the spectrum of the model galaxy (and derived photometry) as the sum of a series of uniform starbursts between each of the time steps in the simulation. When a galaxy is placed in a simulated image at a particular redshift  $z_g$  (implying an age  $t_g$ ), its rest-frame luminosity as a function of wavelength is computed using the star-formation history up to time  $t_g$  using the evolutionary stellar synthesis code GALAXEV by Bruzual & Charlot (2003). Note that the redshift  $z_g$  is not required to be at one of the discrete simulation time steps, since we can integrate the star formation rate from the previous time step to the actual time  $t_g$ . (The need of similar interpolation schemes has also been noticed by Yip 2010). In our reference model, we adopt the Chabrier initial mass function, with a fixed solar metallicity ( $Z = 0.02$ ) and the standard dust model from Charlot & Fall (2000) ( $\tau_\nu = 1$  and  $\mu = 0.3$ ). Our modeling of galaxy spectra is flexible, as we can in principle elaborate this model with additional variables, such as a redshift-dependent metallicity.

### 2.4. Deriving Galaxy Sizes from Dark Matter Halo Sizes

We adjust the size of a model galaxy so that it is always a fixed fraction of the evolving size of its dark matter halo (e.g., Fall & Efstathiou 1980; Kravtsov 2013). We determine the constant of proportionality between the galaxy size and the halo size by comparing their respective  $z = 0$  distributions, as in the halo abundance matching method. However, we match only their medians instead of the full distributions, which suffer from incompleteness in the tails. It is well known that size distributions for halos and galaxies are close to being log-normal (e.g., Shen et al. 2003). Since we choose to

make galaxy size linearly proportional to halo size, the scale parameter and the median subtracted logarithmic distributions of both distributions should be the same. Figure 2 shows the distributions of halo virial radii from Millennium and  $r$ -band half Petrosian flux radii  $R_{50}$  for our main sample of SDSS galaxies from §2.5. The latter has been corrected for incompleteness using the  $V_{\text{MAX}}$  method (Schmidt 1968), as shown with a similar galaxy sample by Taghizadeh-Popp et al. (2012). We find the relation  $R_{50} = 0.022R_{\text{vir}}$ . The dispersions are different (indicating that our assumption is not completely accurate) but are similar enough for our purposes. As in the case of the spectra, we interpolate the galaxy size between discrete time steps to the redshift  $z_g$  of the model galaxy.

### 2.5. Galaxy Image Cutouts from SDSS

Our method places cutouts of real galaxy observations onto our simulated image, which has advantages over using smooth analytic galaxy light profiles. Galaxies often have a clumpy internal structure, which affects source detections. A real galaxy could be detected as two or more separate objects, especially if its surface brightness approaches the image noise level. Real galaxy cutouts recreate this effect and are more realistic than smooth bulge and disk light profiles adopted in previous semi-empirical and semi-analytical models. Of course, this effect is not as important when the apparent galaxy sizes are comparable to the width of the point spread function, as may happen in the high redshift limit.

A database of SDSS galaxy images is used for the cutouts. We select from the SDSS image database the real galaxy that is the closest neighbor to the model galaxy in a multi-dimensional space of galaxy properties. Once the closest matching SDSS galaxy is found, we rescale its flux and size in order to make them equal to those of the model galaxy. No free parameters are fitted or required in this step. The full details of the SDSS data and the selection procedure is described in Appendix B.

One might wonder whether SDSS galaxies are clumpy enough to be accurate models of high-redshift galaxies, since galaxies at higher redshifts tend to be more irregular than local galaxies. The changes in morphology are due both to the shift of optical band filters into the rest-frame ultraviolet for distant objects and also to a higher merger rate and dynamically less-relaxed structures in the early universe.

While these effects are worthy of further exploration in the future, for this paper the SDSS images are a good basis for simulations. Our analysis of galaxy counts and detection efficiencies relies on observations and simulations in the *HST* WFC3/IR F160W filter ( $\lambda = 1.6 \mu\text{m}$ ); this implies that objects with redshifts less than 3 have an SDSS filter (from *griz*) that is at the appropriate rest-frame wavelength, and the different morphologies in the ultraviolet are irrelevant. Moreover, galaxies at redshifts beyond 3 tend to be sufficiently compact that their internal clumpiness has little impact on their detectability. The median FWHM size of detected galaxies with  $z > 3$  in our simulations is 0.3 arcsec, which is only twice the FWHM of the  $1.6 \mu\text{m}$  WFC3 PSF. While there is room for improvement in modeling the internal structure of galaxies, particularly for bluer filters in the  $1 < z < 3$  redshift range, the SDSS cutout images are certainly an

improvement over models that use smooth analytical profiles.

### 2.6. Assembling the Simulated Image

Once model galaxy properties are calculated, we generate pencil-beams through our simulated volume and project them onto the plane of the sky. We then simulate ACS/WFC camera images, with their visible filters, as well as corresponding WFC3/IR images (sampled to the ACS/WFC pixel size), with their infrared filters. We include realistic PSFs for both cameras.

To determine the 3-D structure within these pencil beams, we use a Monte Carlo method. This approach is much simpler and faster than other alternatives, such as the replication of a simulation box much smaller than the depth spanned by the simulated image. We first sample a random redshifts  $z_g$  from a distribution that gives constant comoving volume per redshift interval. Then we randomly select a dark matter halo at  $z = 0$ , choose all of its progenitors found at  $z_g$ , and place them in the simulated image (at redshift  $z_g$ ) according to their relative 3-D spatial positions in the simulation box (interpolating between time steps). Although the large-scale correlations are discarded, we still preserve the short-range correlations between progenitors, while reducing considerably the computation time.

The visual appearance of the model galaxy on the simulated image is given by the best matching SDSS galaxy cutout (Appendix B). We select the SDSS band whose redshifted central wavelength  $\lambda_c$  (to redshift  $z_g$ ) is the closest to the band of the simulated image. Due to the redshift of wavelengths, we end up using the bluest visible SDSS bands to represent most high-redshift simulated galaxies in the visible and infrared *HST* filters, since SDSS lacks the UV and far UV bands that would be more suitable for this redshift regime<sup>3</sup>. Since the  $u$  band is noisy in SDSS, we use the  $g$  band as the bluest bandpass. In fact, all model galaxies placed on the simulated image are represented by a  $g$ -band cutout at  $z > 2$  for ACS/WFC images or  $z > 3$  for WFC3/IR images.

We rescale the flux of the image cutout to match that of the model galaxy. We apply to the model spectrum the effects of redshift, cosmological distance dimming and intergalactic absorption (as in Madau 1995), before applying the photometric filter response.

We rescale the sizes of the galaxy cutouts placed on the simulated image according to one of the following rules:

1. *No size scaling*: The proper size of the original SDSS physical galaxy is left intact, irrespective of the model galaxy size and hence the size of its halo. The physical size is scaled to the apparent size on the image using the angular diameter distance  $D_A(z_g)$ .
2. *Size scaling*: The proper size of the SDSS galaxy is scaled to match the physical size of the model galaxy, which in turn is a fixed fraction of the halo size (as described above). The apparent size is then computed from  $D_A(z_g)$ .

<sup>3</sup> A cross-match between SDSS and *GALEX* might be useful in the future for adding ultraviolet bands to our suite of galaxy cutouts, but that is out of the scope of this exploratory study and analysis.

TABLE 1  
GALAXY EVOLUTION MODELS

Model (short title)	Details
Model 1 ( <i>Reference Model</i> )	<ul style="list-style-type: none"> <li>• Stellar mass-halo mass relation from Guo et al. (2010)</li> <li>• Dust model from Charlot &amp; Fall (2000)</li> <li>• Fixed solar metallicity (<math>Z = 0.02</math>) at all redshifts</li> <li>• Apparent sizes of SDSS galaxy cutouts on image are scaled to the theoretical size predicted by the dark matter halo size</li> <li>• SDSS galaxy cutouts are chosen to be the closest match to the theoretically predicted model galaxy <math>u - r</math> color and stellar mass.</li> </ul>
Model 2	Same as Model 1, but using the Behroozi et al. (2013) SMHM relation evaluated at $z = 0$ .
Model 3	Same as Model 1, but using the Behroozi et al. (2013) redshift dependent SMHM relation.
Model 4	Same as Model 1, but using the a linear SMHM relation $M_s = 0.025 M_{\text{halo}}$ .
Model 5	Same as Model 1, but using no dust model for galaxies.
Model 6	Same as Model 1, but using a fixed very low metallicity ( $Z = 0.0001$ ) at all redshift.
Model 7	Same as Model 1, but without rescaling the intrinsic size of SDSS galaxy cutouts (except for the angular diameter distance scaling, also applied in the reference model).
Model 8	Same as Model 1, but the PetroR50 radius as well as $u - r$ and $M_s$ are used for matching SDSS to model galaxies.

NOTE. — Description of eight different models used for building a simulated universe. Our reference model (Model 1) contains the most plausible parameters and sub-models. Other models are defined by changing one of these parameters at a time.

In the first model, the  $z=0$  size-mass relation of galaxies is preserved at all redshifts, whereas in the second model, the size-mass relation evolves with redshift, driven by the growth of the dark halos. Galaxy sizes tend to be smaller at higher redshifts in the second model due to evolution in the halo sizes.

To add instrumental effects, we convolve with the *HST* point spread function, apply the *HST* instrument efficiency and pixelation, and add noise. The *HST* instrument modeling uses the same software (*pysynphot*, *Tiny Tim*), instrumental parameters and sky background as used in the standard *HST* Exposure Time Calculators, providing a high fidelity model of the real *HST* performance.

### 2.7. Source Detection and Photometry of Simulated Images

The detection, extraction, and photometry of galaxies are performed by running **SExtractor** (Bertin & Arnouts 1996) on the simulated images. Here we directly follow the method and parameters described in Galametz et al. (2013) and designed for the analysis of real *HST* images. The complete output catalog merges **SExtractor** runs using two different detection modes. The Cold mode is used for detecting bright and extended sources, while the Hot mode is optimized for extracting faint and small objects. After extraction, detected or *output* galaxies on the final simulated image are matched (using the detected position and luminosities) to the *input* galaxies on the same image before adding the instrumental effects. This provides a direct measure of the detection completeness by comparing what **SExtractor** detects to what was originally placed on the image.

To compare our simulated galaxies to those from real

galaxy surveys we use **AUTO** magnitudes and Petrosian radii  $R_p$ , as calculated by **SExtractor**. The Petrosian radii of our input galaxy cutouts, as given by the SDSS pipeline, differ from those returned by **SExtractor** on the already simulated images, probably due to different definitions for the radius in the SDSS pipeline and in **SExtractor**. Since we observe a linear offset between the distributions of these radii, we change the input SDSS values to match those from **SExtractor** by using  $\log R_p(\text{SExtractor}) = \log R_p(\text{SDSS}) + 0.41$ .

## 3. RESULTS

The following subsections present our results for eight different models of simulated universes. These models are detailed in Table 1, where the reference model involves the most common choices of parameters as explained in the previous sections, and the seven remaining models vary one parameter of the reference model at a time. In models 2–4 we change the SMHM relation; in models 5–8 we explore extreme values of other models parameter (often deliberately unrealistic values) to test the sensitivity of the observations to these parameters.

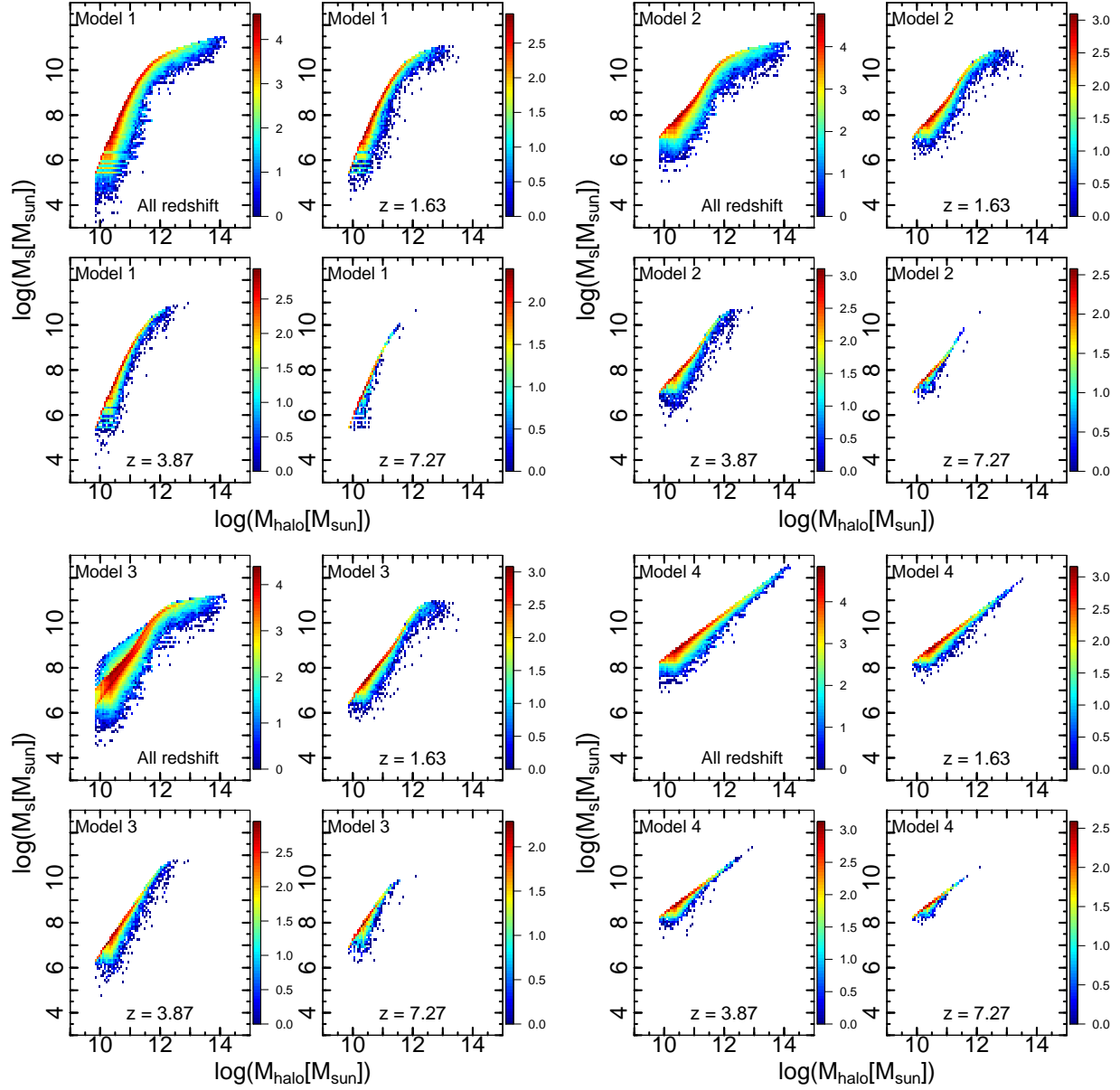


FIG. 3.— Modified stellar mass-halo mass relations for the four models tested in this paper, obtained after retroactively reducing the  $M_s$  values predicted by the one-to-one SMHM relations in Fig. 1 to enforce a monotonically increasing  $M_s$  as a function of time along merger trees. Data from three redshift time steps as well as the combination from all time steps is shown. The colors show the log-scaled number counts in bins of size  $\Delta \log M_{\text{halo}} = 0.06$  by  $\Delta \log M_s = 0.01$ .

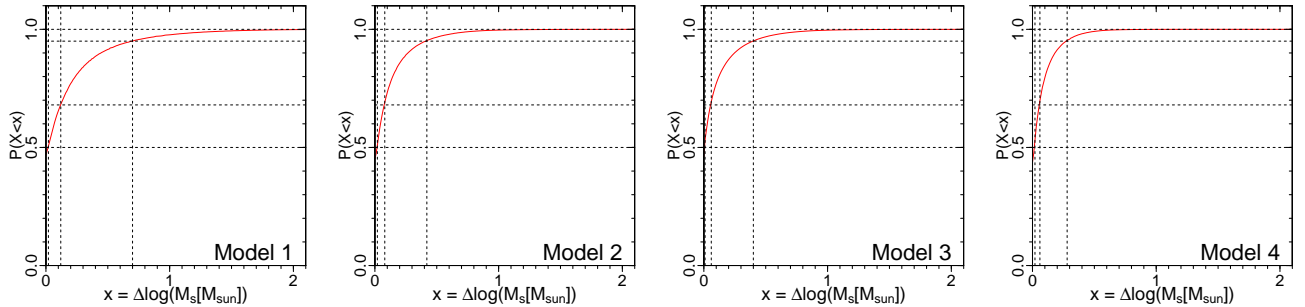


FIG. 4.— Cumulative distributions of the difference between the modified SMHM relation shown in Fig. 3 and the original one-to-one relation from Fig. 1 (values from all redshift time steps are included). The 50%, 67% and 95% quantiles are indicated by dashed vertical lines. About half of the halos in each model have their masses unmodified ( $x = 0$ ).



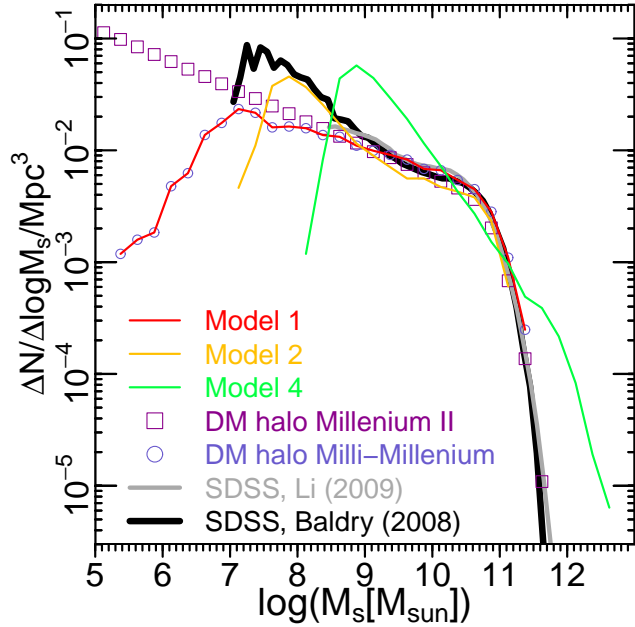


FIG. 5.— Present day stellar mass function for a simulated universe according to the different models of stellar mass-halo mass relations tested in this paper: Model 1 (Guo et al. 2010), Model 2 (Behroozi et al. 2013) and Model 4 (a linear SMHM relation). The open symbols show the stellar mass functions at  $z = 0$  from the milli-Millennium and Millennium II simulations, computed by converting dark matter halo masses into stellar masses using the Guo et al. (2010) relation. Observed stellar mass functions measured from local SDSS galaxies (Baldry et al. 2008; Li & White 2009) are also shown.

### 3.1. Modified SMHM Relations with Natural Intrinsic Scatter

As described in §2.2 and Appendix A, we modified the fixed SMHM relation, selectively reducing the values of  $M_s$  assigned to halos to enforce a monotonically increasing  $M_s$  along merger trees. This leads to the natural dispersion of  $M_s$  values shown in Figures 3 and 4 for the various SMHM relations explored in this paper. For all models, about half of halos do not have their stellar masses modified (meaning that they lie on the imposed SMHM relation). The scatter in the  $M_s$ - $M_{\text{halo}}$  distributions reaches about 0.07–0.12 dex in our simulations, similar to the scatter inferred indirectly from theory and observations (e.g., Reddick et al. 2013; Behroozi et al. 2013). The linear SMHM relation (Model 4) is the least affected by our modifications and shows the smallest dispersion because it lacks the SMHM non-linearity present in the other models. For the non-linear Models 1–3, the scatter is smallest near  $M_{\text{halo}} \sim 10^{12} M_\odot$  because the stellar mass corrections are minimized near the peak of the SMHM relation.

### 3.2. Simulated Universe Models at Low Redshift

We evolve all models of simulated universes to the present day. In this section we compare the model properties with low-redshift observations to test the overall accuracy of our method.

#### 3.2.1. Stellar Mass Functions

Figure 5 compares the stellar mass function of model galaxies at  $z = 0$  to those derived from SDSS. The stellar mass function of the reference model, with its Guo et al.

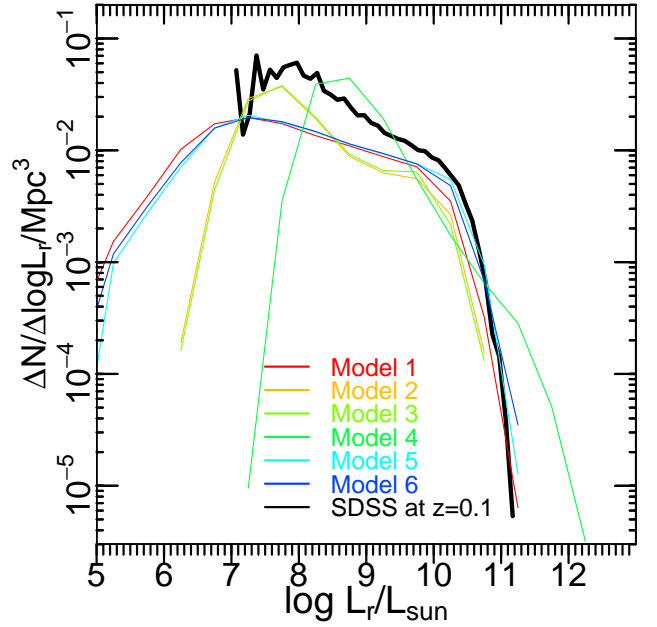


FIG. 6.— Global luminosity functions ( $r$ -band) calculated after evolving our simulated universe to  $z = 0.1$  under six different models. Also shown is the luminosity function of local SDSS galaxies measured by Blanton et al. (2005). Note the similarity with Fig. 5. The downturn in the computed luminosity distributions at low luminosities is due to the finite particle mass resolution in the milli-Millennium simulation.

(2010) SMHM relation, agrees with the observed stellar mass function from Li & White (2009) in the range  $M_s > 10^9 M_\odot$ . That is expected since this SMHM relation was derived from halo abundance matching on mostly the same data. We also confirm that the stellar mass function predicted by the reference model fits perfectly the stellar mass function derived by combining the Guo et al. SMHM relation with the halo mass function from the milli-Millennium simulation, as required by our semi-empirical modeling. However, the stellar mass function of the reference model has an artificial downturn at  $M_s < 10^7 M_\odot$ , which corresponds to the mass resolution of the milli-Millennium simulation in the identification of friends-of-friends groups (composed of a minimum of 20 dark matter particles). Similar downturns are present in the stellar mass functions of the other SMHM relations tested. In contrast, the Millennium II simulation (Boylan-Kolchin et al. 2009), which has a dark matter particle mass 125 times smaller than the mMS, shows a power-law tail at the low-mass end.

The halo abundance matching in the Guo model covered the range  $10^{8.3} < M_s / M_\odot < 10^{11.8}$ , which misses the upturn at  $M_s < 10^9 M_\odot$  that is seen in the more complete SDSS stellar mass function from Baldry et al. (2008) (shown by the black line in Fig. 5). The SMHM relation from Behroozi et al. (2013) (Model 2, yellow line) fits this upturn much better since it was built using the Baldry et al. (2008) stellar mass function.

The linear SMHM relation (Model 4) tracks the approximately  $M^{-2}$  power-law mass distribution of dark matter halos. The proportionality constant for Model 4 was chosen to roughly match the observed stellar mass function around its knee at  $M_s \sim M^*$ . Again, a clear mass resolution cutoff is present at lower stellar masses, also shown in the non-linear relations. This linear SMHM



model is obviously in strong conflict with the observations at both higher and lower masses.

### 3.2.2. Luminosity Functions

Figure 6 compares the simulated and observed luminosity functions at  $z = 0.1$ . To first order, the shapes are Schechter functions. The present-day luminosity functions from our models are similar in shape to their respective stellar mass functions in Figure 5. This is expected since the  $r$ -band luminosity roughly traces the old stellar population that constitutes most of the stellar mass in present-day galaxies (e.g., Bell et al. (2003)). Models 5 (no dust) and 6 (low-metallicity) show good agreement with the Blanton et al. (2005) observed luminosity function in the high-luminosity tail. Since our reference model contains dust and metals, its high-luminosity tail is shifted toward fainter luminosities with respect to those of Models 5 and 6. (Note that the luminosity in the  $r$ -band is reduced by dust absorption even though the bolometric luminosity is conserved.) On the other hand, the flatter slope at low luminosities for these three models mimics the flat tail present in their corresponding stellar mass functions, which is the result of applying halo abundance matching to the stellar mass function of Li & White (2009) as explained earlier. A better fit is obtained for Models 2 and 3 with the SMHM relation from Behroozi et al. (2013), which includes the low-luminosity upturn. The luminosity function derived from the linear SMHM relation for model galaxies tracks the approximately power-law mass distribution of dark matter halos.

The perceptive reader may have noticed that even though semi-empirical modeling promises a perfect match of the predicted to observed universe, the global luminosity function predicted by our reference model does not agree perfectly with the observed luminosity function from SDSS at  $z \sim 0$ . The reason for this is that the  $z \sim 0$  SMHM relation from Guo et al. (2010) is not fully consistent with our method for converting stellar mass into light. They use the stellar mass function derived from Li & White (2009), which is not directly observed but is inferred from the observed SDSS galaxy luminosity function at  $z \sim 0$  and an assumed mass-to-light ratio. On the other hand, our mass-to-light ratio is computed from the dark matter halo masses and the SMHM relation using Bruzual & Charlot (2003) spectral models. We can in principle address this issue by computing our own SMHM relation using an iterative process that compares our measured luminosity functions to the observations. This level of precision is not needed in our present exploratory study, but it will be a useful longer-term goal for our approach.

### 3.3. Simulated *HST* Images and Derived Statistics

In this section, we show simulated *HST* images from our models and test the sensitivity of statistics derived from the images to the model parameters. We focus on the luminosity and size distributions, and we assess both biases in measured parameters and source detection incompleteness. For most tests we compare the perfectly known *input* values of size and luminosity (as given by the models) to the corresponding *output* values measured by **SExtractor** from the images. Our data comprise sim-

ulated visible (ACS/WFC) and infrared (WFC3/IR) images using filters and exposure times appropriate for the GOODS, CANDELS and HUDF surveys. Image sizes and pixel scales are those of a single ACS/WFC exposure (a  $200'' \times 200''$  field with  $0.0495''$  pixels). Note that this image area is small compared with the areas surveyed by many *HST* projects (e.g., GOODS and CANDELS), which encompass many ACS/WFC fields; we considered it appropriate to begin with a more modest sky area for this exploratory project.

#### 3.3.1. Results from the Reference Model

Figure 7 shows a comparison between reference-model simulated and real *HST* ACS/WFC images. At first glance, the spatial distribution of galaxies and associated sizes seem to be very similar. As expected, the HUDF-depth images show that many objects are hidden by noise in the GOODS-depth simulated images.

Figure 8 shows scatter plots of the *input* (true model) values of the apparent sizes and surface brightnesses of both detected (using **SExtractor**) and undetected galaxies in the HUDF-depth image. Most of the detected galaxies can be selected via a cut at  $m_{F160W} \lesssim 29$ , which does not depend strongly on redshift. In the lower panels of Figure 8, which plot surface brightness versus magnitude, it can be seen that there is a small, redshift-dependent population of low surface brightness galaxies that are brighter than the magnitude threshold but nonetheless are not detected.

Figure 9 plots the stellar masses of galaxies versus their input model apparent magnitudes. The stellar mass decreases strongly with increasing redshift. However, an important conclusion from this plot is that even the least massive *detected* galaxies are still generally above the mass thresholds set by both the SDSS survey ( $M_s \gtrsim 10^6 M_\odot$ , Kauffmann et al. 2003) and the milli-Millennium simulation ( $M_s \gtrsim 10^{7.1} M_\odot$ , Guo et al. 2010). Figure 10 shows the typical apparent magnitude values found at the mass completeness limit of the milli-Millennium simulation as a function of redshift. Although the median magnitude initially dims as redshift increases, the curve flattens out at  $m_{F160W} \sim 32$  for  $z > 3$ ; although the galaxies at those redshifts have smaller masses, they also have higher star formation rates and younger populations due to the requirement that their stellar masses be assembled in a short time. That approximately compensates for the cosmological dimming due to the increasing luminosity distance.

*Biases* — As we noted above, Figure 8 shows that a relatively simple cut on the input (model) magnitude of galaxies predicts with reasonable accuracy which galaxies will be detectable in the images. However, detection is not the whole story. It is also necessary to measure the galaxy properties, and those measurements can be biased through complex effects related to the morphology and internal structure of the galaxy. Detection of an object does not ensure that its magnitude, colors, or size can be measured correctly. This is an area where our forward-modeling approach provides more reliable results than previous approaches.

Figures 11 and 12 show strong biases in the **SExtractor**-derived measurements of galaxy sizes and apparent magnitudes. From galaxies detected in the

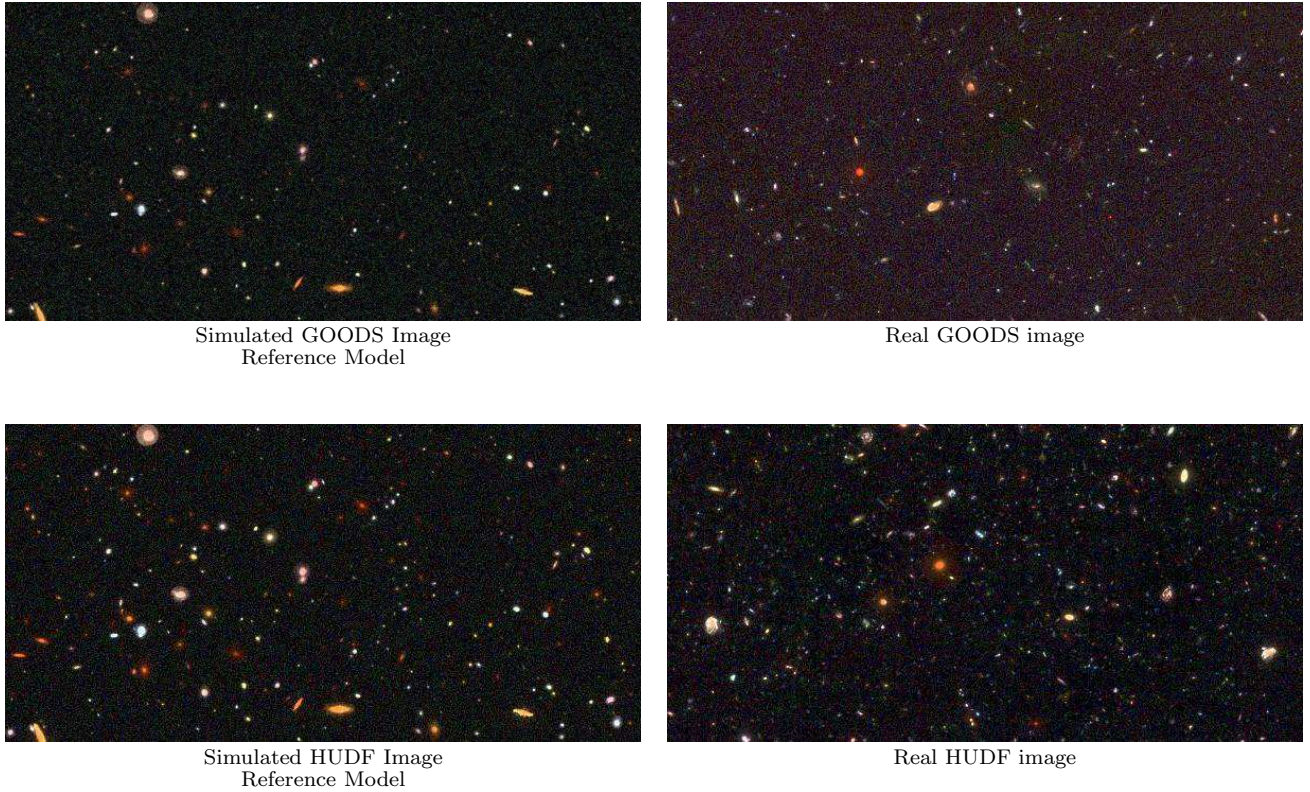


FIG. 7.— Simulated ACS/WFC F850LP+F606W+F435W images built from our reference model (GOODS and HUDF depths), compared to the equivalent real *HST* images. The same exposure times and display contrast are used for the comparison at each depth. The field of view is  $2400 \times 1200$  ACS pixels ( $\sim 1/6$  of the full ACS/WFC field of view).

HUDF-depth simulated image, we compare the differences between the true (*input*) and **SExtractor**-measured (*output*) values of  $m_{F160W}$  and  $\log R_p$ . Our major conclusions are:

1. There is a significant magnitude-dependent luminosity bias, with the measured  $m_{F160W}$  magnitudes on average fainter than the true galaxy magnitudes (Fig. 11). For fainter galaxies, only the compact, high surface brightness nuclei are detectable above the image noise level, while the lower surface brightness extended envelopes are hidden in the noise. This bias is small for bright galaxies, but reaches median values of  $\sim 0.4$  magnitude and extreme values of  $\gtrsim 1$  magnitude at the detection limit. This effect does not depend strongly on redshift.
2. There is also a strong bias in the measured sizes near the magnitude detection limit (Fig. 11). The **SExtractor**-measured sizes are smaller than the original input sizes of model galaxies around  $m_{F160W} \simeq 29$ . The explanation appears to be the same as for the luminosity bias: the detectable part of a faint galaxy is significantly more compact than the true Petrosian radius due to masking of the more extended component by noise. The difference between *output* and *input* values of  $\log R_p$  has a median of 0.15 dex, with maximum values reaching even to 0.8 dex. Note that there is also a Malmquist bias affecting these distributions: faint

extended objects may be detectable only if noise fluctuations make their surface brightness appear brighter than the detection limit.

Figure 11 also reveals a small bias toward larger measured output sizes for sources  $\sim 1$  mag brighter than the detection limit. This bias is largest in the  $z > 6$  redshift bin, where the difference reaches around 0.2 dex, and might be related to intrinsic peculiarities in the way **SExtractor** measures sizes.

These effects are certainly detection biases and not a trend resulting from supposed evolutionary effects in the models. Figure 12 shows a scatter plot of the measured (output) sizes versus measured magnitude for both GOODS and HUDF-depth simulated images. The strong bias in the **SExtractor**-measured sizes at the magnitude detection limit are easily visible at both depths, and the bias begins at a magnitude that is determined by the detection limit rather than at any physically determined luminosity. Note that the underlying images (before adding noise) are exactly the same in these two cases: they are equivalent to observing the same sky region twice with different exposure times. This rules out any artifact introduced by the model. Note how the measured  $R_p$  extends down to values close to the PSF size (FWHM=0.151'' for the F160W band image) at the magnitude detection limit.

We note that the true biases could be even larger than those measured in our simulations. Real galaxy light profiles have extended wings, whereas our galaxy image cutouts only include the light present within two Pet-

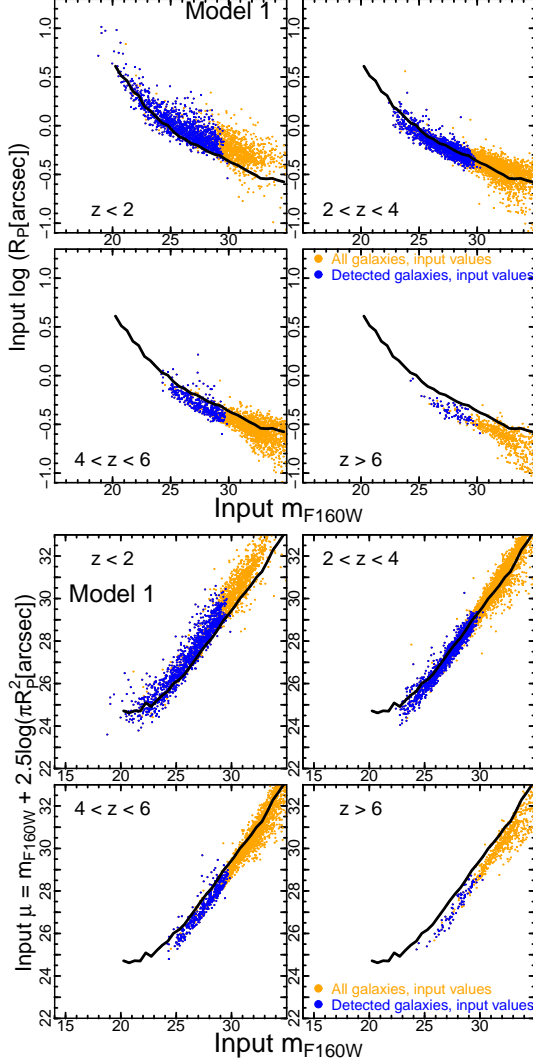


FIG. 8.— *Top*: Log Petrosian radius versus apparent F160W magnitude for the HUDF-depth simulated *HST* image derived from our reference model (Model 1), separated in four redshift bins. Blue points show galaxies detected by **SExtractor**; orange points show undetected galaxies. For all galaxies, the input (model) radii and magnitudes are shown rather than values measured from the images. The black line is the same in all four panels and shows the median of the log  $R_p$  versus magnitude distribution integrated over all redshifts. *Bottom*: Apparent surface brightness  $\mu$  versus magnitude using the same color coding.

rosian radii. According to Strauss et al. (2002), 82% of the light from a de Vaucouleurs profile is contained within this radius, and 99% of light from an exponential profile is included. In addition to these moderate effects, there might be cases when the outer wings of the light profile are much more extended, with surface brightness falling close to  $R^{-2}$ . Then the light in the extended halo would dominate the total luminosity, but such extended emission would certainly not be detectable for faint galaxies, and the biases would be increased. The true radial dependence of the outer wings of galaxies is not currently well constrained, so the amount of light missing from these wings remains an open issue.

**Detection Efficiencies** — The detection efficiency is an important statistic, since it tells us the amount of underlying information that we are losing when observing with

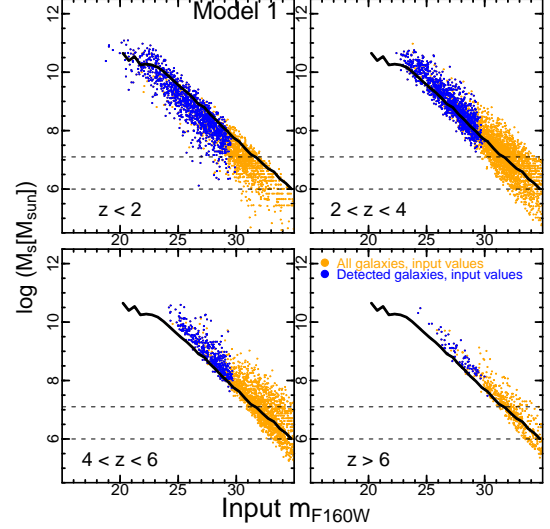


FIG. 9.— Stellar mass  $M_s$  versus apparent F160W magnitude for the HUDF-depth simulated *HST* image derived from our reference model (Model 1), separated in four redshift bins. Color coding is the same as in Fig. 8. The lower dashed line shows the smallest stellar mass for SDSS galaxies in the catalog of Kauffmann et al. (2003) ( $M_s = 10^6 M_\odot$ ). The upper dashed line shows the stellar mass threshold for halos resolved by the milli-Millennium simulation ( $M_s = 10^{7.1} M_\odot$ ) using the Guo et al. (2010) SMHM relation. Note that images from our reference model observed at the HUDF depth are not affected by either threshold, since galaxies located below the thresholds are too faint to detect.

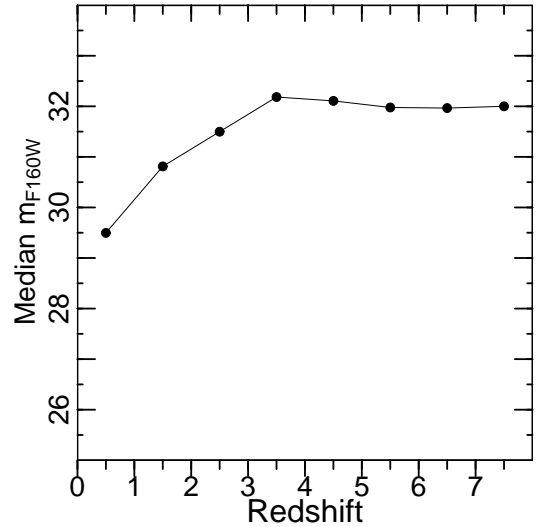


FIG. 10.— Median apparent F160W magnitude as a function of redshift using our reference model for galaxies with stellar masses near the milli-Millennium stellar mass limit of  $M_s = 10^{7.1} M_\odot$  (upper dashed line in Fig. 9). The curve flattens at  $z > 3$  where the youth and high star-formation rates of galaxies compensate for cosmological dimming.

*HST*. In this paper, we consider two different measures of the efficiency: the number count detection efficiency is the fraction of galaxies on the image that are detected in the simulated data, and the light detection efficiency is the fraction of the total galaxy flux in the observing band that is detected. These efficiencies are easily computed from the model images since we know the properties of both the detected and undetected galaxies. Both quan-



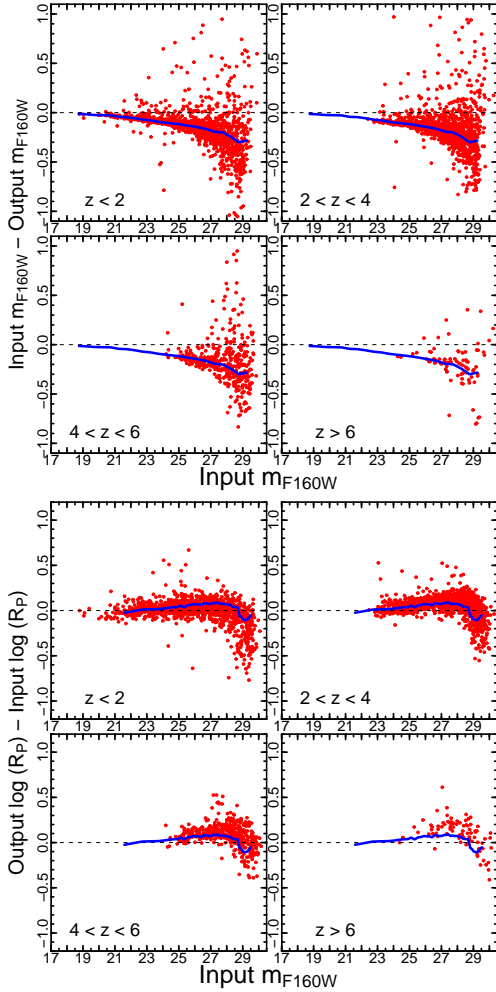


FIG. 11.— *Top*: Magnitude biases: the difference between the true (input)  $m_{F160W}$  magnitude of galaxies and the **SExtractor**-measured output magnitude as a function of the input magnitude. The results for four different redshift ranges in HUDF-depth simulations are shown. Blue lines show the median magnitude differences over all redshifts and are the same in each panel. Points below the dashed line have measured magnitudes that are fainter than the true magnitudes. Fluxes are systematically underestimated for fainter galaxies. *Bottom*: Size biases: same as *top*, but showing the difference between the true input  $\log R_P$  sizes and the **SExtractor**-measured sizes. There is a slight bias toward larger sizes for brighter galaxies, while fainter galaxies have measured sizes that are substantially underestimated. Only the high-luminosity cores of faint galaxies are detected, while the remaining extended emission is lost beneath the noise.

tities can be computed as a function of other parameters such as redshift or apparent magnitude. The number count efficiency is more commonly used but can be ill-defined when one considers the possibility of numerous faint galaxies that are undetected but contribute little stellar mass or light. The light detection efficiency is better behaved, since the integral of light from many faint galaxies is typically a small correction to the light from objects near the knee of the galaxy luminosity function.

The top panel of Figure 13 shows the detection efficiencies for number counts and for F160W-band light at HUDF depth as a function of the model input magnitude of galaxies. Both efficiencies drop sharply to zero at the magnitude detection limit of  $m_{F160W} \simeq 29$ . Interest-

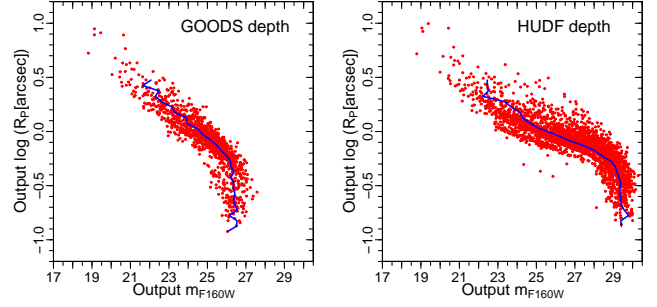


FIG. 12.— Measured (output) size  $\log R_P$  as a function of measured magnitude  $m_{F160W}$  for detected galaxies. The left and right panels show results from simulated images at GOODS and HUDF depth, respectively. The blue lines show the median trend. Note that the tendency to underestimate galaxy sizes at the magnitude completeness limit is evident at both depths, which demonstrates that it is not the product of any peculiarity in the reference model.

ingly, the number count efficiency has the same shape in all redshift bins, showing a slight decline toward fainter magnitudes but remaining above 80% before reaching the detection limit. It reaches values closer to unity only at bright magnitudes in the  $z < 2$  redshift bin. The light detection efficiency has a similar behavior but lower values: it falls to  $\sim 60\%$ – $70\%$  just above the magnitude completeness limit. The lower efficiency for detecting F160W light is due to the magnitude bias discussed above: not only are galaxies undercounted near the detection limit, but the fluxes of detected galaxies near the detection limit are also significantly underestimated (Fig. 11).

The bottom panel of Figure 13 shows the detection efficiencies as a function of redshift. These curves are a bit more complicated to interpret because they are affected by the finite mass resolution of the milli-Millennium simulation. Very low-mass galaxies ( $< 10^{7.1} M_\odot$ ) cannot appear in the simulations, so their contributions to the undetected counts and luminosity are omitted. That means that the computed efficiencies are only upper limits to the real values. This has little effect on the efficiency as a function of magnitude since very few low-mass objects would be brighter than 29th magnitude (Figs. 9 and 10), but it has a significant effect on the redshift-dependent efficiencies since faint galaxies can appear at all redshifts.

Figure 13 shows two attempts to correct the detection efficiencies for the low-mass galaxies. The solid curve simply omits all galaxies fainter than the median magnitude of the lowest mass halos in the milli-Millennium simulation (Fig. 10); the efficiencies plotted are then effectively the fraction of galaxies or light from galaxies brighter than  $\sim 32$  mag, which is an upper limit to the true detection efficiency. The dashed curve instead integrates the light in the extrapolated power-law tail of the faint galaxy luminosity function (Fig. 14) and includes the light of the missing faint galaxies as part of the total flux. This produces a modest correction in the light detection efficiency. Note that a version with extrapolated number counts is not shown because the number count correction factor is much larger (and far more uncertain).

The number count efficiency decreases rapidly from 80% at low redshift to 20% at  $z \sim 7$ . On the other hand, the light detection efficiency drops more slowly, reaching values of  $\sim 50\%$ – $70\%$  at  $z \sim 7$ . The light detection efficiency is greater than the number count efficiency

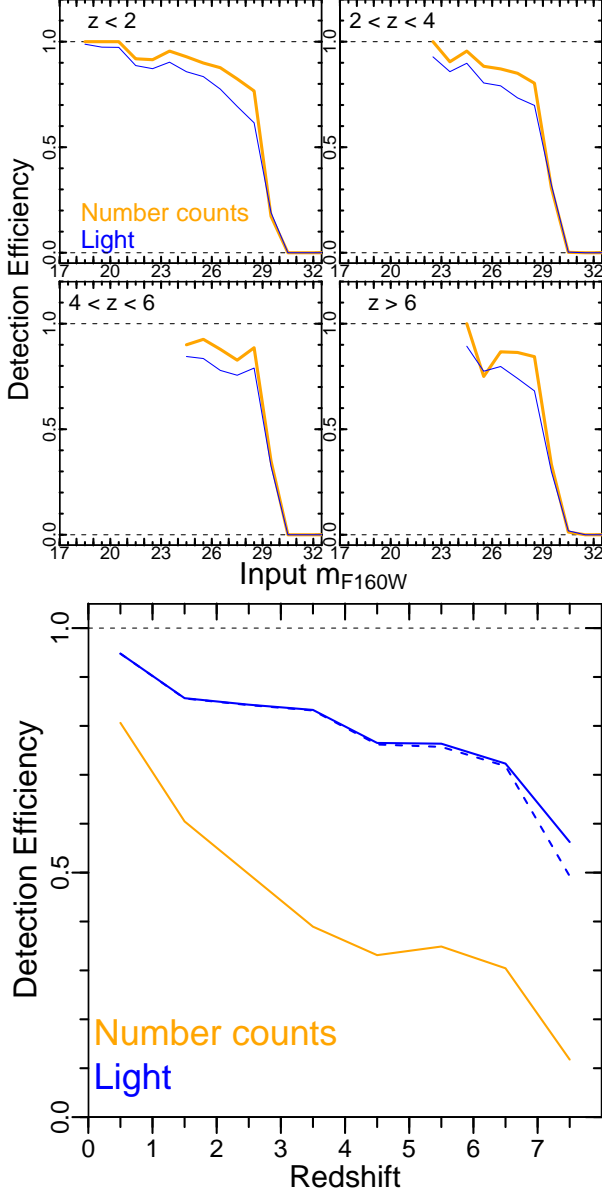


FIG. 13.— *Top*: SExtractor detection efficiency as a function of input  $m_{F160W}$ , measured on a simulated *HST* image at HUDF depth and built from our reference model (Model 1). The number count detection efficiency is the ratio of the galaxies detected by SExtractor to that of all the galaxies placed in the image. The light detection efficiency is the ratio of the output fluxes (F160W band) of detected galaxies as measured by SExtractor to the corresponding model input fluxes of all galaxies placed in the image. Note that light efficiency is smaller than that for number counts because galaxies are not only missed but also have their fluxes underestimated. *Bottom*: Efficiencies as a function of redshift. The solid lines include only galaxies brighter than the median  $m_{F160W}$  at the stellar mass incompleteness limit (Fig. 10). The dashed line uses a power-law extrapolation beyond the mass limit to estimate the light of faint galaxies (Fig. 14).

because every redshift bin includes numerous faint galaxies, and the detected ones (at fixed redshift) are generally the brightest and carry most of the light content of the image.

The correction from including the extrapolated light from faint low-mass galaxies increases at higher redshifts. This can be seen directly in the steepening of the slope

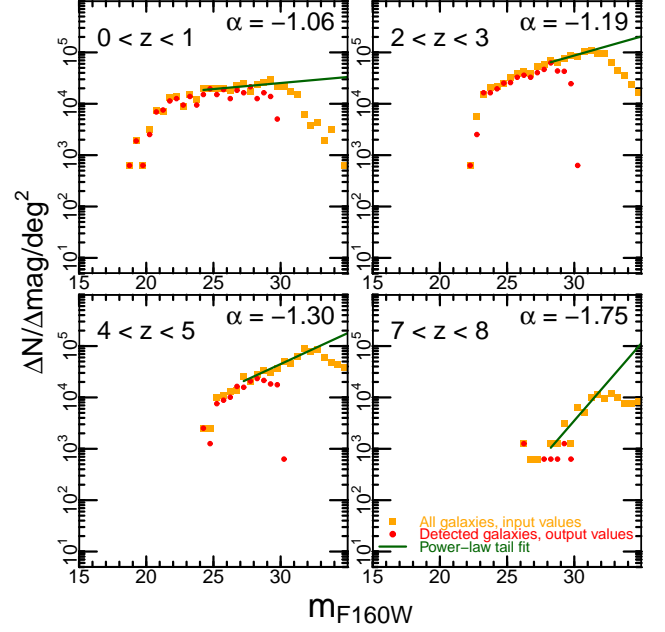


FIG. 14.— Apparent magnitude distribution of our reference model for HUDF depth separated in redshift bins. The green line shows a power-law low-luminosity tail fitted with slope  $\alpha$ . The power-law slope at the faint end tail becomes steeper with increasing redshift.

of the fitted power-law tail at increasing redshifts which changes from  $\alpha \simeq -1$  at  $z < 1$  to  $\alpha = -1.75$  at  $z = 7 - 8$  (Fig. 14). Interestingly, the steep slopes for young galaxies at high redshifts are also found in the present-day universe. Taghizadeh-Popp et al. (2012) isolated similar populations of small, blue galaxies with rapid star formation at  $z = 0$  and also found faint-end luminosity slopes close to  $\alpha \sim -1.6$ .

*Luminosity and size distributions* — The luminosity and size distributions for all galaxies detected on simulated images from the reference model are shown in Figure 15, together with the respective distribution of model input values and SExtractor-measured output values. When compared to the observed luminosities and sizes derived from the CANDELS GOODS-S Multi-wavelength Catalog (Guo et al. 2013b), the SExtractor output values from the reference model (red) agree surprisingly well. For the luminosity distribution, a good fit is found at intermediate magnitudes, but the model predicts slightly too few galaxies at the bright end (possibly affected by sample variance due to the small simulated image area). The drop in the input luminosity distribution at  $m_{F160W} \sim 32$  is an artifact of the finite mass resolution in the dark matter simulation. Since the detection limit of the HUDF-depth image ( $m_{F160W} \sim 30$ ) is 2 mag brighter, we are safe from this artificial incompleteness. The SExtractor size distribution also agrees with the observations, although the model seems to be slightly shifted toward smaller sizes. The bias between the input and output distributions of detected galaxies is also visible in this figure. The HUDF-depth image shows that the peak value of the output  $R_p$  distribution is shifted toward bigger radii by  $\sim 0.1$  dex with respect to the input distribution. Since this bias is not as strong in the GOODS-depth image, we conclude that the ampli-

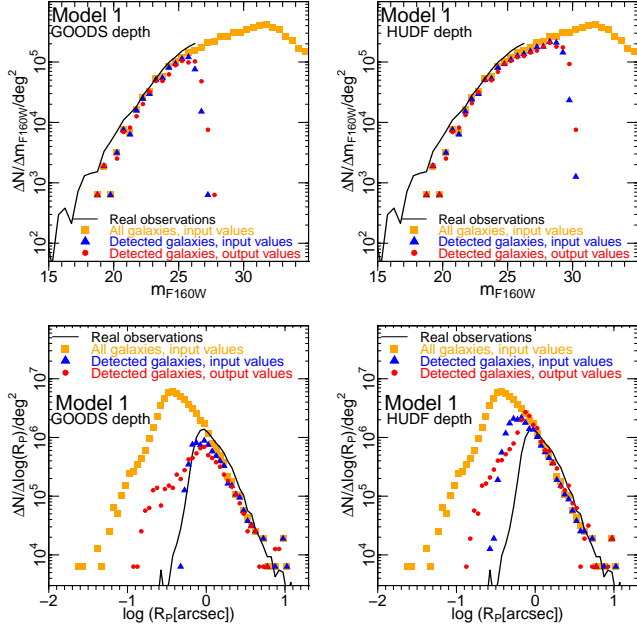


FIG. 15.— Galaxy number counts as a function of apparent F160W magnitude (top) and Petrosian radius (bottom) from simulated *HST* images at both GOODS (left) and HUDF (right) depth using our reference model. The input values of all model galaxies placed in the simulated image are shown as orange squares. The input values for galaxies detected by **SExtractor** are shown as blue triangles, while the output values as measured by **SExtractor** for those detected galaxies are shown as red circles. **SExtractor**-derived distributions are not corrected for incompleteness. Black lines show the actual observed distributions calculated from the CANDELS GOODS-S Multi-wavelength Catalog (Guo et al. 2013b). There is good agreement between the simulated and observed distributions except for the smallest size objects.

tude of the bias depends on the properties of galaxies near the detection limit, which differs in the GOODS and HUDF-depth images. Another interesting feature is that the output size distribution departs from the input size distribution at small values of  $R_p$  (down to the PSF size), where measured sizes for small galaxies are much less than their true sizes. This effect was also discussed above (Fig. 12).

### 3.3.2. Results from Other Models

The statistics derived from simulated images built with other models are qualitatively similar to those of the reference model and follow similar trends. However, the simulated universe is sensitive to changes in the model parameters, and we can easily distinguish variations among the derived statistics for different models.

Figure 16 shows the simulated images from all models. At first glance it is easy to recognize differences between the reference model and the others. For example, some images show a deficit of small galaxies (e.g., Models 2 and 3) or an excess of them (e.g., Model 4). Models 5 and 6 with no dust and low metallicity look brighter, and Model 7 with no size scaling has much larger galaxies.

Figure 17 shows the size versus apparent magnitude for two models that stand out from the others. Model 4, with the linear SMHM relation, predicts higher stellar masses in small-mass halos than the reference Model

1, especially in the high-redshift universe where halos are just starting to assemble. The net effect is to make compact galaxies brighter. Compared with the reference model in Figure 8, a much higher fraction of the galaxies are detected by **SExtractor**, especially in the  $z < 2$  redshift range, since most of the galaxies on the image are brighter than the magnitude detection limit. Model 7, with a non-evolving size-mass relation, has a very different distribution of apparent sizes compared with that of the reference Model 1 and the observed distribution. This is a powerful demonstration that galaxies were smaller in the past, even at fixed mass.

The median apparent magnitudes at the mass completeness limit have different redshift dependences among the models. In Figure 18, most of the models follow the same behavior as Model 1, with the exception of Models 4 and 5. Model 4 has median magnitudes at the mass completeness limit 1.5–3 mag brighter than those of Model 1, since the linear SMHM relation assigns more stellar mass content per unit halo dark matter mass. Model 5, with no dust, brightens at  $4 < z < 7$  in comparison with Model 1, indicating that dust typically dims galaxies about by  $\sim 1$  mag in the redshifted filter bandpass. All the models, however, flatten at high redshift as discussed for the reference model.

Figure 19 shows detection efficiencies for all models as a function of both magnitude and size. The number count efficiency as a function of magnitude varies for all models similarly to that of the reference model, declining slowly to 80% just above the magnitude detection limit and then dropping dramatically, irrespective of redshift. The light detection efficiency as a function of magnitude also shows a close similarity among the models, dropping to 60%–70% just above the magnitude detection limit.

Regarding the number count detection efficiency as a function of size, most models have high efficiency (80%–90%) for larger objects with a sharp drop at input radii of  $\sim 1''$ . The drop is due to smaller objects also having smaller fluxes so that they are closer to the detection limit. There are, however, two models that stand apart. The linear SMHM relation in Model 4 makes compact, low-mass galaxies that are more massive and brighter than those in Model 1, and this greatly enhances the detectability of smaller objects. As a consequence, the detection efficiency stays above 50% at input sizes down even to  $0.1''$  for  $z > 4$ . At the other extreme, Model 7 (with the non-evolving size-mass distribution) has larger sizes and much lower detection efficiency at high redshift compared to the other models. The larger size distribution is seen because galaxy sizes are not scaled in proportional to the halo sizes. Consequently high redshift galaxies are large fuzzy objects that are strongly suppressed in the images by the  $(1+z)^4$  cosmological surface brightness dimming, and very few of them (10%–20%) are detected. The smaller sizes of galaxies at high redshift in most of the models are essential to making them detectable. The light detection efficiency as a function of size shows similar effects, although the differences for Models 4 and 7 are less dramatic.

The detection efficiencies as a function of redshift in Figure 20 are only upper limits to the real values, since we are missing halos smaller than the mass completeness limit in the dark matter simulation. We calculate these efficiencies using only galaxies that are above the median



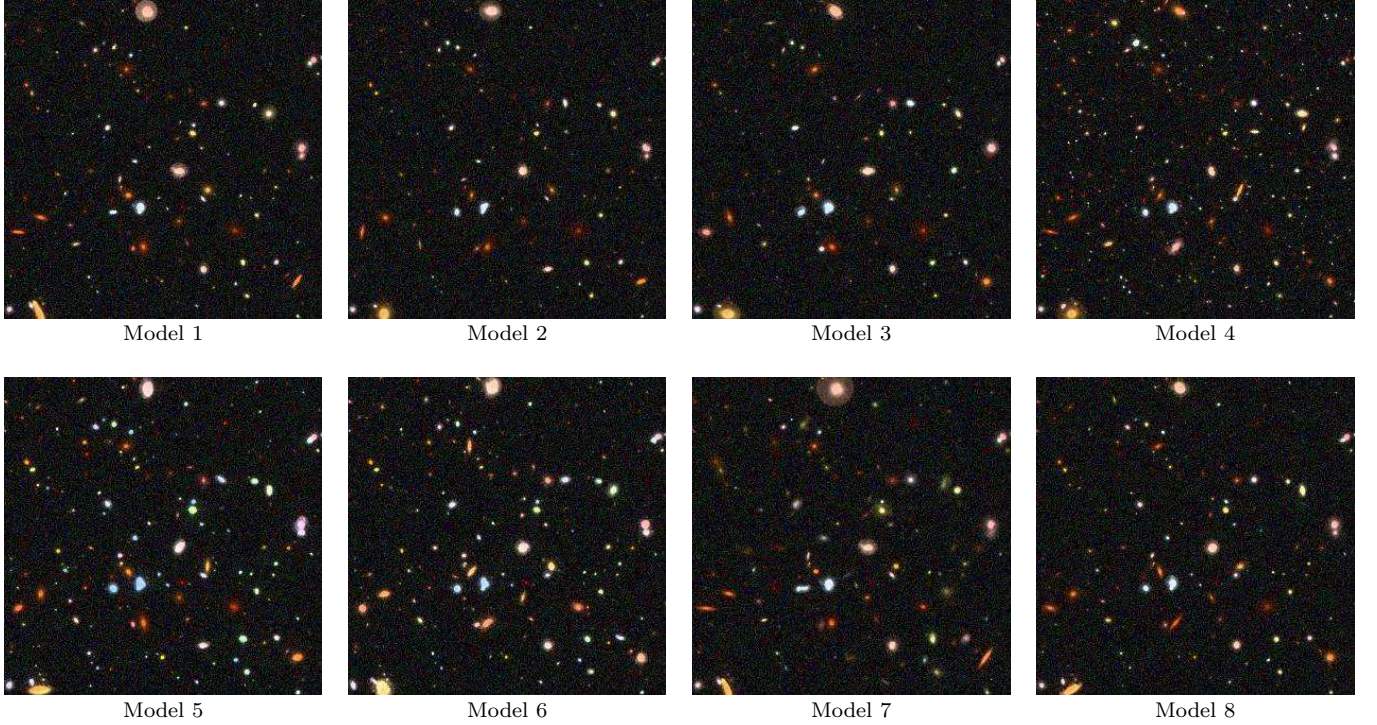


FIG. 16.— Simulated ACS/WFC F850LP+F606W+F435W images (HUDF depth) derived from for all models explored in this paper. The same exposure times and display contrast are used for the comparison at each depth. The field of view is  $1200 \times 1200$  ACS pixels ( $\sim 1/12$  of the full ACS/WFC field of view). Changes in the distribution of luminosity and sizes are apparent for different models.

magnitude set by the simulation mass resolution. The distributions for different models are qualitatively similar although there are some significant variations. The efficiency amplitudes depend strongly on the model and on how compact and luminous the galaxies are, especially in the case of the number count efficiency. For example, Model 4, with its more compact galaxies, shows by far the highest number count detection efficiencies,  $> 60\%$  at all redshifts. The light detection efficiency is higher than the number count efficiency for all models. It is noteworthy that Model 5, with no dust, shows the highest light detection efficiencies at  $z > 4$ . These experiments show that the efficiencies depend on details of the models and that understanding them is key to inferring the physics of galaxy formation from observations.

Figure 21 shows luminosity functions, which are especially suitable for exploring the effects of our different models on the simulated images. Changing the SMHM relation modifies the stellar mass distribution across redshift, which can be seen directly as a change in the apparent luminosity functions. According to Figure 5, the linear SMHM relation (Model 4) predicts a much higher  $M_s$  at a given  $M_{\text{halo}}$  than the Guo et al. relation, especially for halos with  $M_{\text{halo}} \lesssim 10^{11} M_{\odot}$ . That shifts the peak of the luminosity function toward brighter magnitudes compared with the reference model. Since the galaxies are brighter, more of them are detected by **SExtractor** or seen by eye (e.g., Figs. 16 or 17). With the Behroozi et al. SMHM relation,  $M_s$  is higher than with the Guo et al. SMHM relation at small values of  $M_{\text{halo}}$ , but lower at high  $M_{\text{halo}}$  (for any redshift). The net effect is a shift of the peak to brighter magnitudes, but at the expense of fewer galaxies just brighter than the peak. At  $z = 0$ , the

Behroozi et al. SMHM relation is similar to that of Guo et al., so the luminosity function of Model 2 is closer in shape to that of Model 1. Galaxies in Model 5 (with no dust) are, as expected, more luminous than in the reference model, in some cases  $\sim 0.7$  magnitudes brighter in the range  $22 \lesssim m_{\text{F160W}} \lesssim 25$ . Model 6 (with low metallicity) behaves similarly to Model 5, but the magnitude shift is not as large. These 2 models also give good fits to the observations. The last 2 models share the same input  $z = 0$  luminosity function as the reference model, since only the size of galaxies are modified. Therefore, Model 8, which uses  $R_{50}$  in the matching between model and SDSS galaxies, has a luminosity function at  $z = 0$  similar to that of Model 1. However, Model 7 is slightly different at the onset of incompleteness, since here galaxy sizes are not scaled and are therefore larger than in the reference model. The galaxy sizes affect the surface brightnesses and so are influential in determining the detectability of faint galaxies.

The size distributions in Figure 22 mostly behave in the same way as in the reference model, except for Models 4 and 7. For Model 4 (linear SMHM relation), the peak of the output size distribution shows a larger bias toward bigger sizes (by  $\sim 0.2$  dex) compared to the input distribution. Note also that the output size distribution for smaller detected galaxies always falls below that of the input distribution. The input sizes of the smallest detected galaxies extend well below the FWHM of the PSF ( $0.151''$ ), but those bright enough to be detected have **SExtractor** sizes comparable to the FWHM. (We have not modified the **SExtractor** sizes to remove the effects of the PSF.) The size distribution for Model 7 is, not surprisingly, very different from the other distribu-

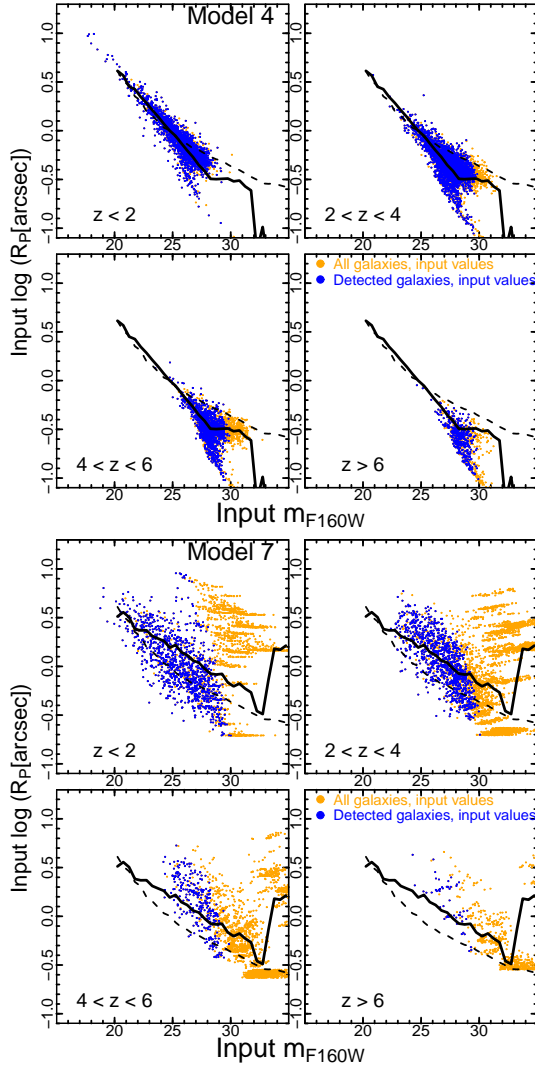


FIG. 17.— Petrosian radius versus apparent F160W magnitude for the HUDF-depth simulated *HST* image derived from Models 4 (top) and 7 (bottom), separated in four redshift bins. Colors are the same as Fig. 8. The solid line shows the median values for these models, while the dashed line shows the median for the reference model for comparison. Small galaxies are given a higher luminosity in Model 4; the large galaxy sizes in Model 7 lead to many galaxies being undetected due to low surface brightnesses.

tions, since its galaxies lie on a non-evolving size-mass relation rather than having their sizes rescaled by the evolving sizes of their halos. That results in many large, faint galaxies at high redshift that are difficult to detect.

#### 4. COSMIC STAR FORMATION RATES

The cosmic star formation rate density (SFRD, the mass of stars formed per unit time and per unit comoving volume) and its evolution with redshift have played a key role in studies of galaxy formation (see Madau & Dickinson 2014, and references therein). We have postponed consideration of the SFRD until now because, although this relation is derived from observations and is often portrayed as an “observed” relation, it is unsuitable for direct comparison with our models. In previous studies (e.g., Behroozi et al. 2013), predictions of the SFRD are compared with observations in the theoretical domain, i.e., by combining observed galaxy

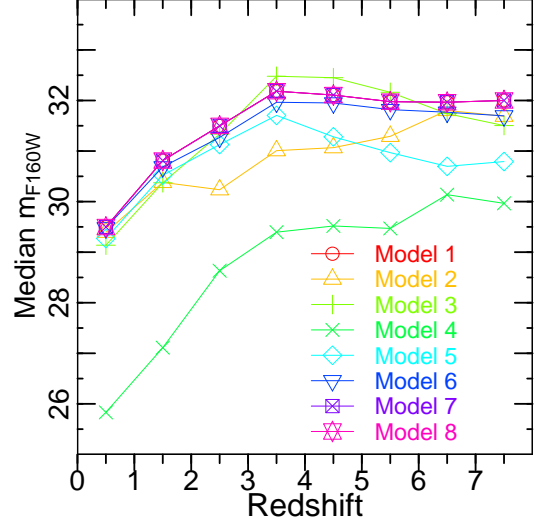


FIG. 18.— Median apparent F160W magnitude of galaxies having stellar masses near the simulation mass incompleteness limit of  $\log M_s/M_\odot = 7.1$ , shown for galaxies in different redshift bins. Data is shown for all the models explored in this paper.

counts and colors with corrections for dust absorption but without corrections for missing light at low luminosity and surface brightness. We argue instead that it is better to project theoretical models into the observational domain by creating simulated data and making comparisons directly with the observed quantities (“forward modeling”). However, a complete study using that approach is beyond the scope of this paper.

Nonetheless, a comparison between our model properties and SFRD values from the literature is illuminating. Figure 23(a) shows the SFRD in our reference model using the SMHM relation from Guo et al. (2010). The solid red line is the SFRD that results from our approach of enforcing a monotonically increasing stellar mass in halo merger trees by retroactively suppressing star formation (see §2.2 and Appendix A). Observations from the compilation of Behroozi et al. (2013) are also shown. The model SFRD lies above the data points at high redshift ( $z > 4$ ) but below them at low redshifts ( $z < 2$ ).

Figure 23(b) shows the SFRD in our model using the redshift-dependent SMHM function from Behroozi et al. (2013). Since Behroozi et al. (2013) forced their model to match the observed SFRD, one might expect that this SMHM function would also be consistent with the observations. However, while our model SFRD (solid red line) is similar to the observations at high redshift ( $z > 6$ ), it is still too low at lower redshifts.

We have identified two significant effects that can raise the SFRDs in our models. First, additional star formation is required to replace the stellar mass that is lost as massive stars reach the end of their lifetimes and die. We compute the additional star formation from the simple approximation given in Eqn. (14) of Behroozi et al. (2013) for the fraction of mass lost from a single starburst as a function of age; this function is integrated over time to determine the ongoing star formation rate with recycled material. The resulting enhanced SFRD, shown in Figure 23 as the dashed blue line, is increased by factors ranging from 1.5 at  $z \sim 3$  to 2.5 at  $z \sim 0$ . This recycling effect is important and should be incorporated into future models, but it does not fully explain the difference

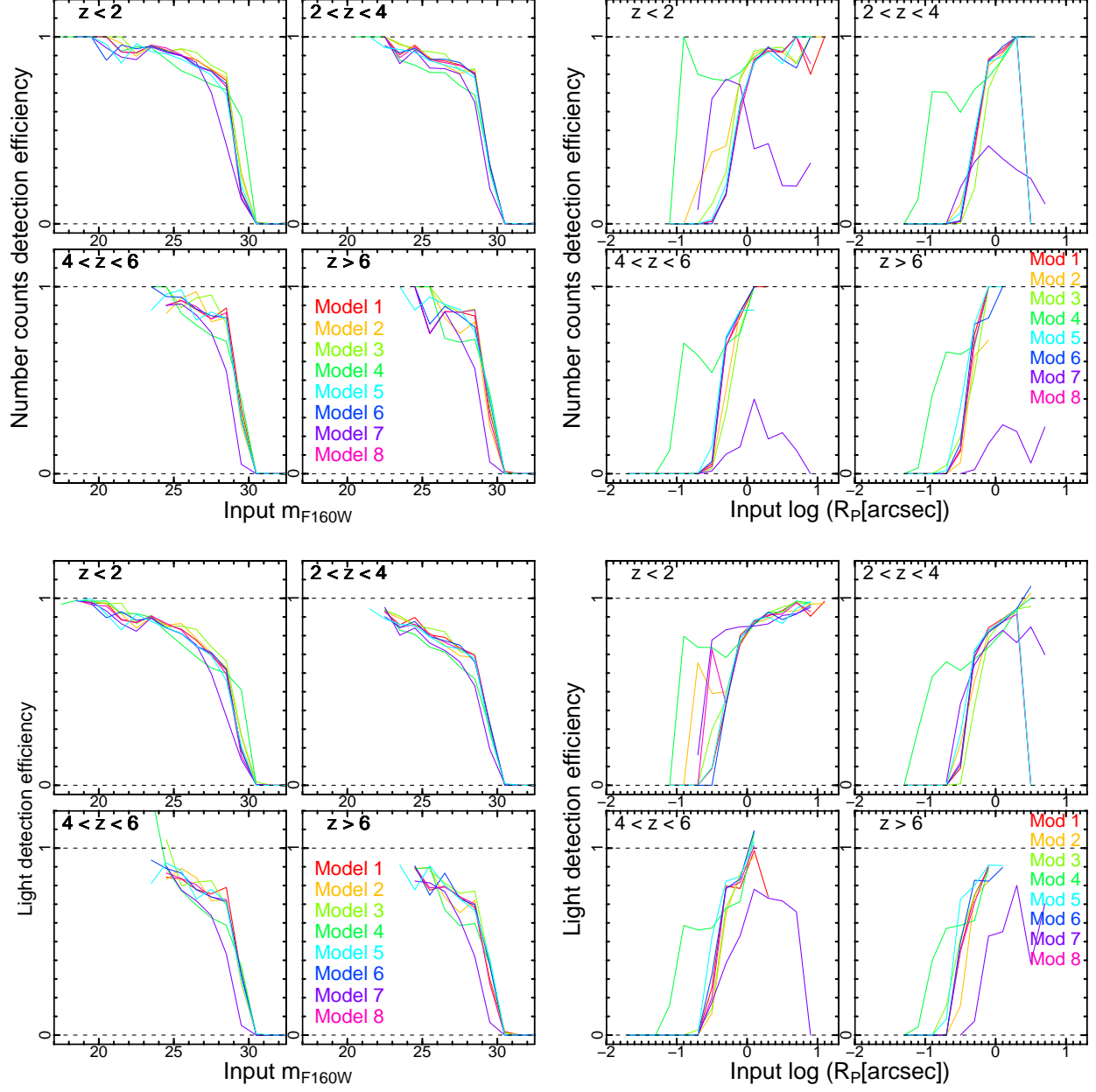


FIG. 19.— **SExtractor** number count (top row) and light (bottom row) detection efficiencies as a function of the input  $m_{F160W}$  magnitudes (left) and Petrosian radii (right) of detected galaxies in the HUDF-depth simulated *HST* image, shown for each of the models explored in this paper. Note that the efficiency is lower for small galaxies because smaller galaxies are also fainter.

between the computed SFRDs and the observations.

The second potentially important effect is the ejection of stars from galaxies during merging. This is a crucial feature of the Behroozi et al. (2013) calculation: the fraction of stars that escape from galaxies is an adjustable parameter. Those stars are then subsequently replaced by additional star formation. This parameter enables fitting both the observed SFRD and the galaxy masses in massive cluster-scale halos. Most of the intergalactic stars end up in clusters of galaxies and hence contribute to the diffuse intracluster light (ICL).

To include the possibility of star formation enhancement through ICL, we adopt a more conservative procedure. Our standard approach with star formation sup-

pression reduces the star formation rates in merger trees to ensure that the stellar mass of galaxies never decreases. An alternative model is to allow all galaxies to form the stars required by the SMHM relation, and then to eject the excess mass (if any) to the ICL. The dot-dashed green lines in Figure 23 show the enhanced SFRDs that result from this procedure. With this addition, the model SFRD for the Behroozi et al. (2013) SMHM relation has been increased by another factor of 2 and agrees reasonably well with the observations at all redshifts.

Does this agreement imply that there *must* be a large fraction of stellar mass ejected to the ICL in order to match the observed SFRD? Probably not. In the



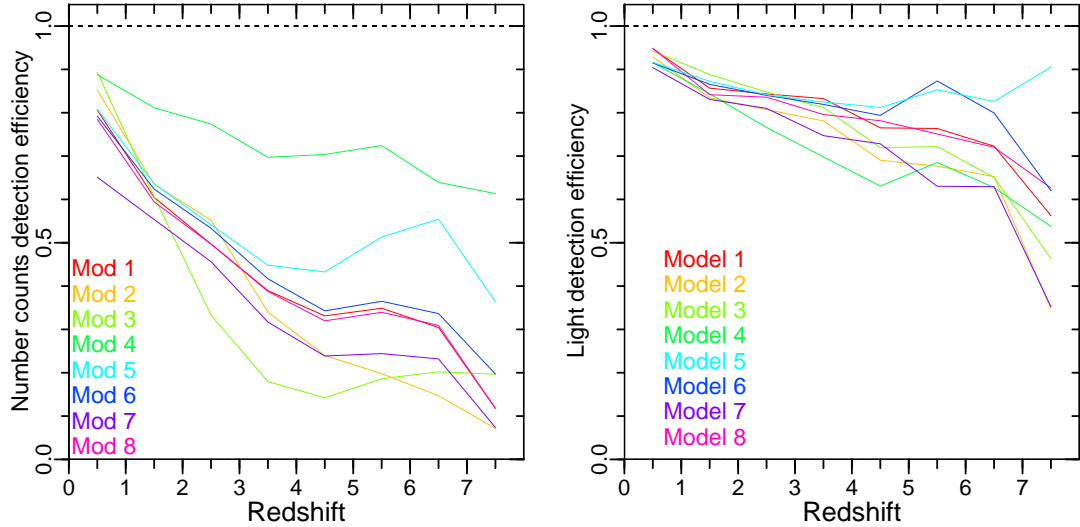


FIG. 20.— Detection efficiencies as in Fig. 19, but plotted as a function of redshift. We include only galaxies brighter than the median  $m_{F160W}$  at the stellar mass incompleteness limit, as shown in Fig. 18.

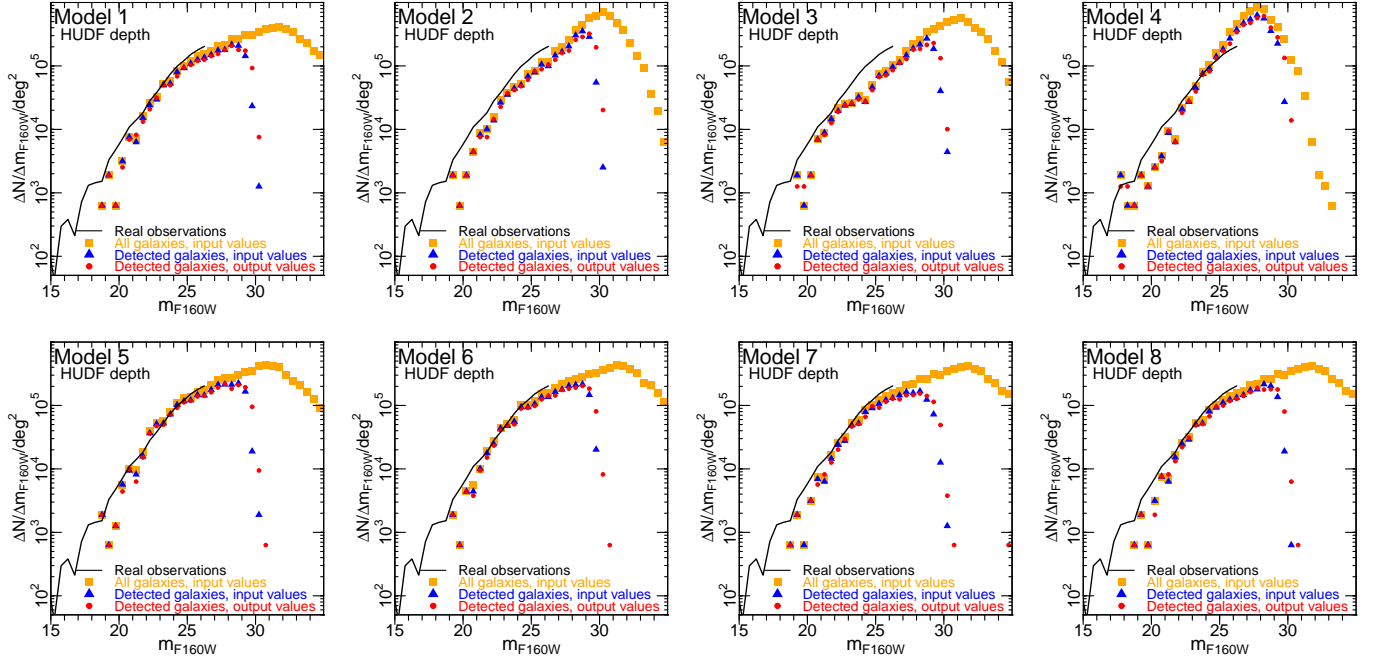


FIG. 21.— Apparent F160W magnitude distribution from simulated *HST* images at HUDF depth for all models tested in this paper. Symbols are the same as in Fig. 15. The biggest differences in the shapes of the simulated distributions come from the use of different stellar mass-halo mass relations (Models 1–4). Removing dust or metal content (Models 5 and 6) mostly shifts the distribution toward brighter magnitudes.

Behroozi et al. (2013) computations, 30% of the stellar mass in the universe lies outside galaxies, with the ICL mass fraction being higher in clusters (P. Behroozi, private communication). Such a large fraction of extragalactic stars may be in conflict with observations of the ICL, which suggest ICL stellar mass fractions closer to 10% (e.g., Mihos et al. 2005; Zibetti et al. 2005; Krick & Bernstein 2007; Gonzalez et al. 2007; Presotto et al. 2014; Montes & Trujillo 2014). A model that relies on hiding much of the stellar mass outside of galaxies in order to enhance the SFRD may conflict as strongly with the observations as one that does not

generate much intracluster light but has a lower SFRD.

Instead of treating the inferred SFRD and ICL as known quantities, a better approach would be to apply the forward modeling methodology discussed in this paper: from simple theoretical models of galaxy masses and star formation rates, create simulated observations, including the SFRD and the ICL. Then the comparison between the models and the observations should be carried out entirely in the observational domain. It seems quite plausible that a consistent model can be created that fits the observed galaxy masses, observed SFRD indicators, and measured ICL properties; such a model will

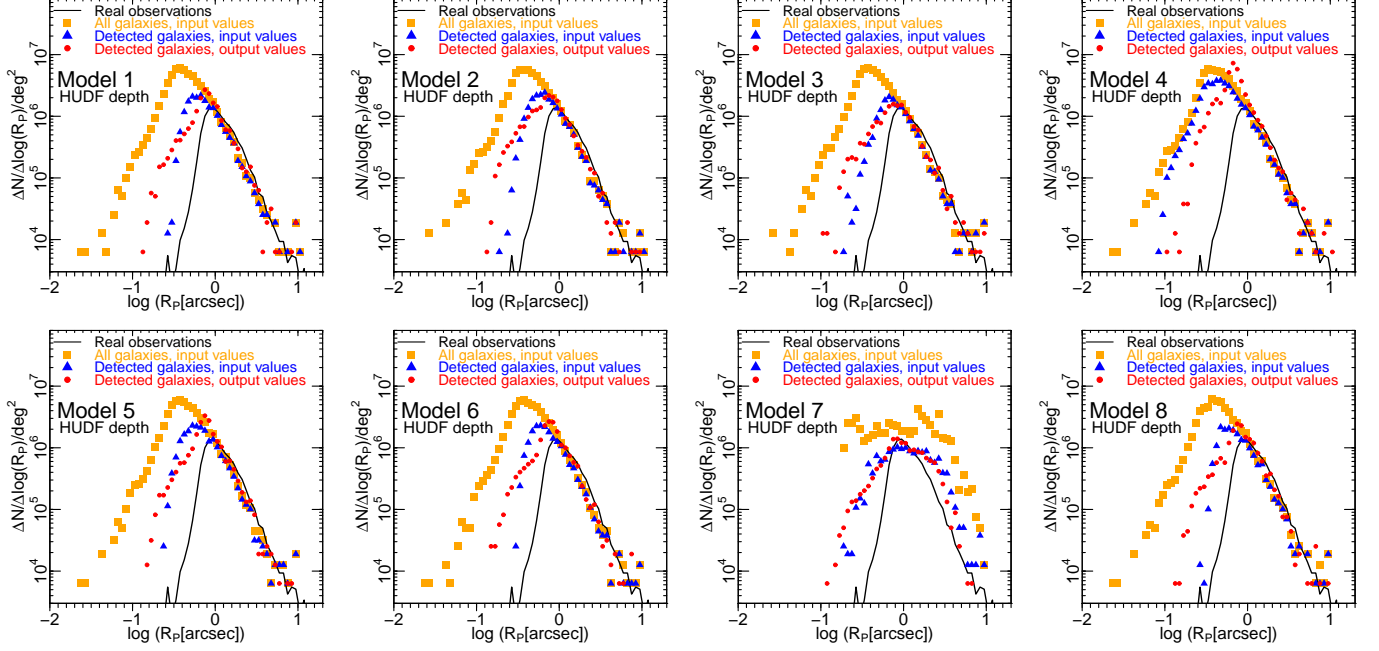


FIG. 22.— Size functions from simulated *HST* images at HUDF depth for all models explored in this paper. Symbols are the same as those in Fig. 21. Reasonably good agreement for larger objects is found with the real observations (black line) except for Model 7, which has larger galaxy sizes that do not scale with the halo size evolution.

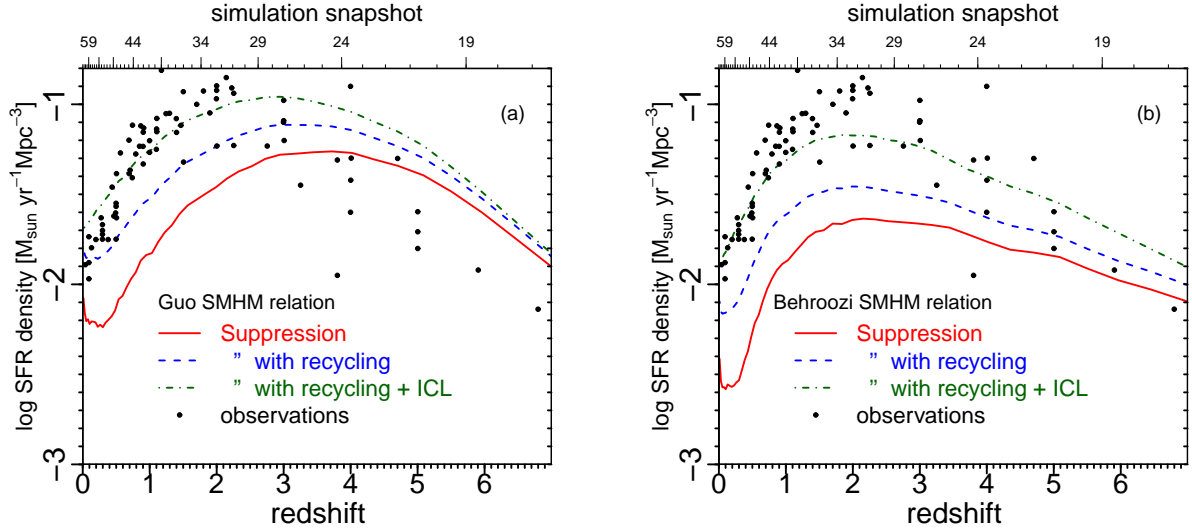


FIG. 23.— Cosmic star formation rate density (SFRD) as a function of redshift. (a) Reference SMHM model from Guo et al. (2010). (b) Redshift-dependent SMHM model from Behroozi et al. (2013). The black dots show observed SFRDs compiled by Behroozi et al. (2013). The solid red line is the SFRD for our model with suppression of past star formation to create a monotonically increasing stellar mass in halo merger trees. The dashed blue line includes the additional star formation from instantaneous recycling of mass lost from shorter-lived more massive stars to maintain the stellar mass. The dot-dashed green line results from assuming that rather than suppressing star formation to enforce a monotonically increasing stellar mass, all halos form the stars required by the SMHM relation but the excess stellar mass is ejected from the halos to form intracluster light (ICL). The models including ICL fit the observations best but require that most stars reside in the ICL rather than in galaxies (see text for discussion).

not necessarily demand a very large stellar mass in the ICL.

## 5. DISCUSSION

### 5.1. Summary of Results

This paper demonstrates that a credible simulated universe, consistent with deep *HST* images, can be constructed using only a few basic assumptions and a small number of parameters. The simplicity of our model, in

contrast with the complexity of most other models of galaxy evolution, enables robust comparisons with the observed universe. A key element of this comparison is to project our models of evolving galaxy populations into the observational domain and to extract measurements from the simulations using the same tools as used to analyze the real images (“forward modeling”). Since our simulated *HST* images include all relevant cosmological, instrumental, and selection effects, they can be compared

directly with real *HST* images. In order to simulate the clumpiness and internal structure of galaxies, we cut out images of SDSS galaxies as templates for our model galaxies (instead of the commonly used smooth Sérsic profiles), with their fluxes and sizes rescaled to reflect the properties of model galaxies in our simulations.

The key assumption of our theoretical modeling is that most of the information needed for a first order match between the simulated and observed universes is already encoded in the gravitational dynamics of dark matter halos, as derived from cosmological  $N$ -body simulations. In this semi-empirical approach, we express the stellar mass and size of a model galaxy as a function of the mass and size of its host halo. This effectively avoids any detailed modeling of complex baryonic physical processes, in contrast to semi-analytical and hydrodynamical simulations, with their larger number of assumptions and parameters. Our semi-empirical models are based on statistical matching between the distribution of halo mass and size measured in the  $N$ -body simulation to the distribution of stellar mass and size for real galaxies at  $z = 0$ , thus guaranteeing a good match between the present-day simulated and observed galaxy populations. For the evolution of galaxy populations, we adopt several simple models for the redshift dependence of the stellar mass-halo mass (SMHM) relation. We also show that the evolution of the luminosities and spectra of galaxies can be modeled, to good approximation, using the star formation histories implied by the growth of the stellar mass of each galaxy along the merger tree of its host halo. The galaxy spectra are determined by convolving the star formation histories with stellar population synthesis models.

The analysis of simulated *HST* images is a powerful tool for comparing the predictions from different models of galaxy evolution. By comparing directly in the observational domain, we can decide which choices of parameters make an observable difference and which do not. Our reference model assumes a non-evolving SMHM relation and non-evolving solar metallicity and dust content. Despite these simple assumptions, it provides a good match to real *HST* images, particularly when comparing the luminosity and size distributions. Including plausible redshift-dependence in the SMHM relation does not radically alter the simulated *HST* images. In contrast, a much less plausible, linear SMHM relation, with the stellar mass proportional to the halo mass, leads to a far greater abundance of compact, high-luminosity galaxies in low-mass halos at high redshift. From this and our other models, we conclude that the stellar mass efficiency per unit halo mass should indeed peak at stellar masses around  $M_*$  and decrease for smaller and higher masses. Metallicity and, especially, dust have a strong effect on the observed galaxy properties, with their luminosities increasing by up to 0.7 mag when removing dust or metals from the galaxies. From the analysis of galaxy sizes, we conclude that galaxies must be smaller in the past. A simple linear scaling between galaxy and halo sizes provides a good match between the size distributions of simulated and real *HST* images. If there were no evolution in the sizes of galaxies, the deep *HST* images would appear almost empty.

We also find that the measured values of size and luminosity of galaxies in the simulated images are strongly biased. **SExtractor** underestimates the luminosities and

sizes of simulated galaxies especially around the magnitude detection limit, as the extended low surface brightness components of galaxies are lost in the image background noise. These biases vary among the models, depending primarily on the size-luminosity relation of galaxies. For example, our model with a linear SMHM relation predicts more light for small, faint galaxies, which makes them easier to detect compared with our reference model.

The detection efficiency of galaxies, measured by comparing the number and luminosities of detected galaxies in the simulated images to those for all model galaxies, also reveals some interesting results. For the reference model, the number detection efficiency declines slowly with magnitude as objects get fainter to  $\sim 80\%$  just above the detection limit and it then drops more rapidly. This behavior is similar at low and high redshifts, since it depends only on whether galaxies are bright enough to pass the magnitude cut. The fraction of light recovered from galaxies, on the other hand, falls considerably faster with magnitude; it is  $\sim 60\text{--}70\%$  right above the detection limit and then drops sharply. The reason for this is that **SExtractor** not only fails to detect faint galaxies but also underestimates the fluxes of the ones it does detect. Note that although the model with a linear SMHM relation behaves similarly as a function of magnitude; it has a much higher detection efficiency at small sizes, since it assigns more luminosity to the small, high-redshift galaxies, making them easier to detect. The fraction of missing light may be underestimated in our simulations because they truncate the luminosity profiles of galaxies at two Petrosian radii.

The redshift dependence of the detection efficiencies is also interesting but requires some additional considerations. The numerator of the efficiency (i.e., the number of detected galaxies or the total light detected) is measured with reasonable accuracy. However, the denominator (the total number or luminosity of galaxies) is not well determined because our images are missing galaxies with masses below the resolution of the milli-Millennium simulation. We address this issue by fitting the power-law tail of the luminosity function, and estimate the missing light by extrapolating the fitting function toward zero luminosity. Our measurements for the reference model show that the fitted power-law slope becomes steeper at higher redshift, changing from  $\alpha \sim -1$  at  $z < 1$  to  $\alpha = -1.75$  at  $z = 7 - 8$ . Since the slopes are shallower than the divergence value  $\alpha = -2$ , the extrapolated missing light is always finite and the fraction of missing light is modest in our case. Indeed, the light detection efficiency drops from  $\sim 90\%$  at small redshifts to only  $\sim 50\%$  at  $z = 7 - 8$ . These values depend sensitively on the slope of the luminosity function, which in turn depends on the dark matter halo mass distribution. Since the power-law tail of this mass distribution has a slope of  $\alpha = -2$  (confirmed both by theory and simulations), it would not be difficult to find models with suitable combinations of SMHM relations and mass-to-light ratios that predict a power-law slope of the luminosity function closer to  $\alpha = -2$  or even steeper, resulting in very small detection efficiencies. We demonstrated this by our model with a linear SMHM relation, which presents a lower light efficiency than models with more plausible SMHM relations. The total number of galaxies, on the other hand, diverges for



slopes steeper than the limit  $\alpha < -1$ . Since our simulated universe presents steeper slopes, we conclude that the number counts detection efficiency as a function of redshift cannot be accurately measured using the milli-Millennium simulation at most redshift.

### 5.2. Future Directions

The main goal of this paper was to develop some first-generation simulations of deep *HST* images using semi-empirical models of evolving galaxy populations. In this spirit, we have tried to strike a balance between models that are realistic enough for meaningful conclusions and models that are simple enough for computational efficiency and ease of interpretation. Indeed, we regard the simplicity of our models, with relatively few assumptions and parameters, as a definite virtue in a preliminary exploration such as this. Now that this initial analysis has been successfully concluded, it is appropriate to consider how our approach can be enhanced for greater physical realism and accuracy. In the remainder of this section, we outline several directions for future studies of this type.

A relatively straightforward enhancement of our models would be to base them on dark-matter simulations with larger comoving volumes and smaller particle masses, such as the Millennium II (Boylan-Kolchin et al. 2009) or Bolshoi (Kyplín et al. 2011) simulations. The larger volume would permit a more accurate simulation of both the small and large-scale distribution of galaxies in deep images than is possible with the milli-Millennium simulation. In particular, it should be possible to lay down light cones through the simulation volume to compute galaxy distributions rather than relying on sampling the halo distribution as we do in this paper. Such simulations, in addition to providing direct estimates of correlation functions and other clustering statistics on large scales, will provide estimates of the variance in counts and other properties of galaxies in smaller fields. The higher mass resolution of larger dark matter simulations will enable the modeling of galaxy populations to lower masses and luminosities. This is especially important for the simulation of *JWST* images, which will reach much fainter magnitudes than the *HST* images considered here. The extension of model galaxy populations to lower masses will also improve estimates of detection efficiencies for the counts and light of galaxies, which depend on extrapolations of luminosity functions below the detection thresholds.

It would be also worthwhile to make simulations with a larger suite of SMHM relations. The resulting simulated *HST* images could then be compared with observed images and a goodness of fit assigned to each of

these SMHM relations (by e.g. maximum likelihood). The requirement that the models satisfy constraints on the SFRD and ICL (§4) could be added to the procedure at this stage. In this way, the “best” SMHM relation and confidence regions around it could be determined. As a byproduct, such statistical tests would indicate how much useful information *HST* images really contain about galaxy formation and evolution. In particular, we would like to know whether the evolution of the SMHM relation can be pinned down uniquely or whether substantially different SMHM relations lead to similarly good fits in comparison with *HST* observations. This issue has important theoretical implications; different SMHM relations presumably reflect differences in the physical processes in galaxy formation and evolution. This issue also has practical implications, because simulations like those presented here could be used to guide future observing strategies, with different telescopes, cameras, and filters, to determine the SMHM relation most efficiently and robustly and to resolve ambiguities in the models.

Another improvement would be to allow the metal and dust content of model galaxies to evolve with redshift. Our results, based on non-evolving metal and dust content, show that differences in these quantities are readily apparent in simulated *HST* images. A physically plausible scheme for evolving the metal and dust content should be based on the star formation and thus the metal enrichment history of each galaxy in the model. Unfortunately, the stellar metallicity and ISM dust optical depth also depend on the evolution of the ISM of each galaxy, including inflows and outflows, and these cannot be specified without introducing additional assumptions and parameters. This is why we have neglected the evolution of the metal and dust content in the present exploratory study. Nevertheless, such effects could and probably should be included in future studies, provided one is willing to pay the price of extra assumptions and complexity.

We are grateful for support of this project by the STScI Director’s Discretionary Research Fund. We thank Henry Ferguson and Michael Peth for help on running *SExtractor*, Ching-Wa Yip for help on running *GALAXEV* and Victor Paul for helping with Data-Scope maintenance. We thank Massimo Stiavelli and Jason Tumlinson for helpful discussions in the early phases of this project and Peter Behroozi for helpful input in the later phases.

## APPENDIX

### A. ENFORCING A SELF-CONSISTENT, MONOTONICALLY INCREASING STELLAR MASS IN THE MERGER TREE

We have developed a self-consistent and recursive method that ensures a monotonic increase in the stellar mass content of dark matter halos across their merger trees. This retroactive suppression mechanism functions in the following way: when a halo is measured to decrease its current  $M_s$  value, we suppress accordingly the value of  $M_s$  in its progenitor halos located in the closest previous time steps, which consequently causes scatter away from the one-to-one SMHM relation. First, we start with a root halo picked from the collection  $\{h_i\}_{i=1}^{i=N}$  of all  $N$  halos found in the last ( $k$ th) time step in the simulation (most likely to be at  $z = 0$ ), and compute  $M_s = M_s(M_{\text{halo}})$  for all halos in its merger tree using the one-to-one SMHM relation. Then we pick its progenitors located in the previous ( $k - 1$ )th time step and verify that  $\Sigma M_{s,\text{prog}} \leq M_{s,\text{root}}$ . If not, we reduce the stellar masses of these progenitors (proportionally to their masses), so that  $\Sigma M_{s,\text{prog}} = M_{s,\text{desc}}$  holds. We continue decreasing the  $M_s$  values in halos of all the closest

previous time steps until reaching the  $j$ th time step ( $j < k$ ), where  $\Sigma M_{s,\text{prog}} \leq M_{s,\text{root}}$  holds for all progenitor halos located at the  $(j - 1)$ th time step. This process is repeated recursively and backward in time throughout the merger tree of the root halo, with each one of its progenitors playing the role of the root halo, that is, each progenitor goes later under the same process that modifies  $M_s$  values along its own (smaller) merger tree. All the previous steps are then repeated for the next root halo in  $\{h_i\}_{i=1}^N$  until the whole dark matter simulation is traversed. Evidently, the optimal case would be to have the  $k$ th time step located (if available) at sometime far enough in the future, so that all values of  $M_s$  at  $z = 0$  are modified and stabilized.

## B. GALAXY IMAGE CUTOUTS FROM SDSS

This appendix describes the procedure used to select SDSS galaxy image cutouts that represent model galaxies on our simulated *HST* images.

As a repository of galaxy images, we use the SDSS Data Release 10 (York et al. 2000; Ahn et al. 2014). This data archive (a MS-SQL Server database available online via CasJobs<sup>4</sup>) is suitable for our needs, as it provides imaging and spectroscopy of  $\sim 10^6$  galaxies as well as many other derived physical properties.

We use in particular the Main Galaxy Sample (MGS, Strauss et al. 2002), which spans a rich variety of galaxy types over a sky area of  $7930 \text{ deg}^2$ . These galaxies form a flux-limited sample, with an  $r$ -band Petrosian apparent magnitude limit of  $m_r \leq 17.77$ . We define our sample in the redshift range of  $[z_1, z_2] = [0.01, 0.2]$ , with the peak of the redshift distribution located at  $z \sim 0.1$ . We consider clean **science primary** galaxies only on calibrated images having the **photometric** status flag. We discard suspicious detections and objects with deblending and interpolation problems, as well as objects whose spectral line measurements and properties are labeled as unreliable<sup>5</sup>. Our main sample contains  $\sim 400,000$  galaxies.

The properties available for the MGS that we use in this paper are the photometry in the *ugriz* bands, in particular model magnitudes for computing the colors (Stoughton et al. 2002). A measure of the galaxy size is given by the (redshift insensitive)  $r$ -band Petrosian radius  $R_P$  (Petrosian 1976) and its less noisy proxy  $R_{50}$  (the radius encircling 50% of the Petrosian flux). The galaxy stellar mass  $M_s$  is also available; it was obtained from spectral analysis at MPA and JHU<sup>6</sup>, as detailed by Kauffmann et al. (2003).

We extract the galaxy cutouts from 50 TB of 5-band,  $2048 \times 1489$  pixel SDSS image frames using parallel processing in the Data-Scope,<sup>7</sup> a computing facility designed specifically for data-intensive applications (Szalay et al. 2012). As a first step, we denoise the images using the anisotropic diffusion method (Perona & Malik 1990), which is particularly useful for the more noisy  $u$  and  $z$  bands. This leaves the galaxy outline and internal structure intact, since the smoothing is done in the direction locally parallel to the edges or borders. Multi-band images are registered to the same reference frame using cubic spline interpolation.

We extract individual galaxy cutouts from the original images, considering only what is included inside an aperture of radius  $2R_P$  centered at each galaxy. To avoid the influence of neighboring objects, we do not use galaxies where the sum of fluxes from all neighbors that overlap the aperture exceeds 1% of the galaxy flux. This leaves us with a total of  $\sim 270,000$  galaxies in the repository.

We select from the SDSS image database the galaxy that is the closest neighbor to the model galaxy in the multi-dimensional space of galaxy properties. For this paper, we use two sets of parameters to select matching SDSS galaxies:

1.  $u - r$  color and  $\log M_s$
2.  $u - r$  color,  $\log M_s$  and  $\log R_{50}$

Other schemes using additional parameters were tried with very similar results. Each property is mean-subtracted and normalized by the standard deviation before doing the matching. The  $u - r$  color tracks the flux difference before and after the  $4000\text{\AA}$  break, and is a good indicator of age. To compare photometry, the (evolved) rest-frame spectrum of the model galaxy is redshifted to the median of the SDSS redshift distribution ( $z = 0.1$ ), and then convolved with the  $u$  and  $r$  filters. Using the properties from a simulated universe based on our reference model (§3), we find that the median of the rms error over all properties derived from the second matching scheme ( $\log \text{rms} = -0.85$ ) is bigger than that of the first scheme ( $\log \text{rms} = -1.18$ ), since there is one more variable to match ( $\log R_{50}$ ). However, the individual median rms error for  $\log R_{50}$  in the second matching scheme is  $\sim 1$  dex smaller than that of the first. A good compromise is to use the first matching scheme to get a smaller overall rms error, but then to manually rescale the SDSS galaxy size to match the model galaxy size as described in §2.6. This approach is used as part of our reference model as well.

## REFERENCES

- |  |  |
|--|--|
| <p>Ahn, C. P., Alexandroff, R., Allende Prieto, C., et al. 2014, ApJS, 211, 17</p> <p><sup>4</sup> <a href="http://casjobs.sdss.org">http://casjobs.sdss.org</a></p> <p><sup>5</sup> More details in <a href="http://sdss3.org/dr11/algorithms">http://sdss3.org/dr11/algorithms</a></p> <p><sup>6</sup> <a href="http://www.mpa-garching.mpg.de/SDSS">http://www.mpa-garching.mpg.de/SDSS</a></p> <p><sup>7</sup> <a href="http://idies.jhu.edu/datascope">http://idies.jhu.edu/datascope</a></p> | <p>Baldry, I. K., et al., 2008, MNRAS, 388, 945</p> <p>Behroozi, P. S., Conroy, C., &amp; Wechsler, R. H. 2010, ApJ, 717, 379</p> <p>Behroozi, P., Wechsler, R. H., Conroy, C. 2013, ApJ, 770, 57</p> <p>Bell, E. F., McIntosh, D. H., Katz, N., &amp; Weinberg, M. D. 2003, ApJS, 149, 289</p> <p>Bertin, E. &amp; Arnouts, S. 1996, A&amp;AS, 117, 393</p> |
|--|--|

- Blanton M. R., Lupton R. H., Schlegel D. J., et al., 2005, *ApJ*, 631, 208
- Blaizot, J., Wadadekar, Y., Guiderdoni, B., et al., 2005, *MNRAS*, 360, 159B
- Bouche, N., Dekel, A., Genzel, R. et al. 2010, *ApJ*, 718, 1001
- Bouwens, R. J., Illingworth, G. D., Oesch, P. A., et al., 2014, *arXiv:1403.4295v1*
- Boylan-Kolchin, M., Springel, V., White, S. D. M., Jenkins, A., & Lemson, G. 2009, *MNRAS*, 398, 1150
- Bruzual A., G. & Charlot, S., 2003, *MNRAS* 344, 1000
- Charlot, S. & Fall, S. M., 2000, *ApJ*, 539, 718
- Conroy C., Wechsler R. H., Kravtsov A. V., 2006, *ApJ*, 647, 201
- Conroy, C., & Wechsler, R. H. 2009, *ApJ*, 696, 620
- Devriendt, J., Rimes, C., Pichon, C., et al. 2010, *MNRAS*, 403, L84
- Fall, S. M., Efstathiou, G., 1980, *MNRAS*, 193, 189
- Galametz, A., Grazian, A., Fontana, A. et al. 2013, *ApJS*, 206, 10
- Gonzalez, A. H., Zaritsky, D., & Zabludoff, A. I. 2007, *ApJ*, 666, 147
- Guo, Q., White, S., Li, C., Boylan-Kolchin, M. 2010, *MNRAS*, 404, 1111
- Guo, Q., White, S., Angulo, R. E., Henriques, B., et al. 2013a, *MNRAS*, 413, 101
- Guo, Y., et al. 2013b, *ApJS*, 207, 24
- Guo, Q., & White, S. 2014, *MNRAS*, 437, 3228
- Kauffmann, G. et al., 2003, *MNRAS*, 341, 33
- Krick, J. E., & Bernstein, R. A. 2007, *AJ*, 134, 466
- Klypin, A. A., Trujillo-Gomez, S., & Primack, J., 2011, *ApJ*, 740, 102
- Komatsu, E., Smith, K. M., Dunkley, J. et al., 2011, *ApJS*, 192, 18K
- Kravtsov, A. V., 2013, *ApJL*, 764, L31
- Lemson, G., Springel, V., 2006, in *ASP Conf. Ser.* 351, *Astronomical Data Analysis Software and Systems XV*, ed. C. Gabriel, C. Arviset, D. Ponz & E. Solano (San Francisco, CA: ASP), 212
- Li C., White S. D. M., 2009, *MNRAS*, 398, 2177
- Lotz, J., Jonsson, P., Cox, T. J., & Primack, J. R. 2008, *MNRAS*, 391, 1137L
- Madau, P. 1995, *ApJ*, 441, 18
- Madau, P., & Dickinson, M. 2014, *ARA&A*, 52, 415
- Mihos, J. C., Harding, P., Feldmeier, J., & Morrison, H. 2005, *ApJ*, 631, L41
- Montes, M., & Trujillo, I. 2014, *ApJ*, 794, 137
- Moster, B. P., et al. 2010, *ApJ*, 710, 903
- Moster, B. P., Naab, T., & White, S. D. M. 2013, *MNRAS*, 428, 3121
- Mozena, M. W., 2013, PhD thesis Univ. California, Santa Cruz, CA
- Overzier, R., Lemson, G., Angulo, R. E., et al. 2013, *MNRAS*, 428, 778
- Perona, P. & Malik, J. 1990, *IEEE Transactions on Pattern Analysis and Machine Intelligence*, 12(7):629-639
- Petrosian, V. 1976, *ApJ*, 209, L1
- Presotto, V., Girardi, M., Nonino, M., et al. 2014, *A&A*, 565, AA126
- Reddick, R., et al. 2013, *ApJ*, 771, 30
- Schmidt, M. 1968, *ApJ*, 151, 393
- Spergel, D. N., Verde, L., Peiris, H. V., et al. 2003, *ApJS*, 148, 175
- Springel, V., White, S. D. M., Jenkins, A. et al. 2005, *Nature*, 435, 629
- Stoughton, C., Lupton, R. H., Bernardi, M., et al., 2002, *AJ*, 123, 485
- Shen, S., Mo, H. J., White, S. D. M., et al. 2003, *MNRAS*, 343, 978
- Strauss, M. A., Weinberg, D. H., Lupton, R. H., et al. 2002, *AJ*, 124, 1810
- Szalay, A. S., Church, K., Meneveau, C., Terzis, A., Zeger, S., 2012, MRI: The Development of Data-Scope - a multi-petabyte generic data analysis environment for science, available at [wiki.pha.jhu.edu/escience\\_wiki/images/7/7f/DataScope.pdf](http://wiki.pha.jhu.edu/escience_wiki/images/7/7f/DataScope.pdf)
- Taghizadeh-Popp, M., Heinis, S., Szalay, A. S., 2012, *ApJ*, 755, 143
- Vale A., Ostriker J. P., 2004, *MNRAS*, 353, 189
- Yip, C.-W. 2010, *AJ*, 139, 342
- York, D. G., Adelman, J., Anderson, J. E., Jr., et al., 2000, *ApJ*, 120, 1579
- Zibetti, S., White, S. D. M., Schneider, D. P., & Brinkmann, J. 2005, *MNRAS*, 358, 949